



High resolution digital outcrop model of faults and fractures in caprock shales, Konusdalen West, central Spitsbergen

Peter Betlem^{a,b}, Thomas Birchall^a, Gareth Lord^a, Simon Oldfield^c, Lise Nakken^{a,b,d}, Kei Ogata^e, and Kim Senger^a

^aDepartment of Arctic Geology, The University Centre in Svalbard, P.O. Box 156, N-9171 Longyearbyen, Svalbard, Norway

^bDepartment of Geosciences, University of Oslo, Sem Sælands vei 1, 0371 Oslo, Norway

^cDanish Offshore Technology Centre, Technical University of Denmark, Elektrovej, Building 375, 2800 Kgs. Lyngby, Denmark

^dDepartment of Earth Sciences, Royal Holloway, University of London, Egham Hill, Egham TW20 0EX, United Kingdom

^eDepartment of Earth, Environmental and Resource Sciences, Università degli Studi di Napoli Federico II, Via vicinale cupa Cintia 21, Complesso Universitario di Monte S. Angelo, Edificio L, 80126 Napoli, Italy

Correspondence: Peter Betlem (peterbe@unis.no)

Abstract. Structure-from-motion (SfM) photogrammetry has become an important tool for quantitative characterisation of outcrops. Digital outcrop models (DOMs) allow for the mapping of stratigraphy and discontinuous structures like folds, faults and fractures from cm to km scale and provide solutions that are difficult to constrain through subsurface data alone. With pristine, treeless exposures, the outcropping strata in Svalbard, Arctic Norway, hold exceptional potential for analogue studies and are ideally suited for the acquisition of high-resolution DOMs. We here present the acquisition, processing and integration of the Konusdalen West digital model data set, comprising both DOM and derived digital terrain model (DTM) data. Drone-based image acquisition took place over two weeks in July and August 2020. Fifteen differential GNSS control points were used to georeference and quality assure the model, five of which functioning as reference checkpoints. SfM processing of 5512 acquired images resulted in high-confidence, cm-scale resolution point clouds, textured mesh (DOM), tiled model, orthomosaics, and a DTM. The confidence-filtered dense cloud features a median inter-point distance of 1.57 cm and has an average point density of 3824.9 points m⁻². For the five checkpoints, the dense cloud features root mean square errors of 2.0 cm in X, 1.3 cm in Y, 5.2 cm in Z, and 5.7 cm in XYZ. Drops in point confidence and point density are mainly found in areas with reduced image densities, and on the backside of boulders. Increased confidences and densities are present along the western flank of the Konusdalen West outcrop, where a fault-fracture network in mudstone-dominated stata is best exposed and photographed most extensively.

The Konusdalen West DOM and DTM cover a 0.12 km² area and span a 170 m elevation difference. The mean of the altitude of the checkpoints versus elevation of the dense cloud-derived DTM differed by less than a cm. The dense cloud-derived DTM closely matches an existing lower-resolution reference DTM of the area. The DOM covers the upper two-third of the mudstone-dominated Late Jurassic-Early Cretaceous Agardhfjellet Formation. The Agardhfjellet Formation and its time-equivalents are regional cap rocks for CO₂ sequestration and petroleum accumulations both on the offshore Barents Shelf and onshore Svalbard. Faults, formation members and established marker beds can be traced in the high-resolution model and have been used for the stratigraphic integration. Additional structural measurements and observations were taken in June 2021 to place



the data in the geological context. Top and side-view orthomosaics feature maximum resolutions of 8 mm per pixel, enabling the mapping of fractures and other sub-cm features. The Konusdalen West digital model data set, together with the extensive
25 drill cores through the same section near Longyearbyen, forms an ideal starting point for the generation of high-resolution, outcrop-truthed geomodels that are suitable for numerical modelling of fluid flow and appraisal of the regionally important caprock. Data described in this manuscript can be accessed at Norstore under <https://doi.org/10.11582/2022.00027> (Betlem, 2022b).

1 Introduction

30 Structure-from-motion (SfM) photogrammetry has become a cost- and time-effective tool for the digitisation of outcrops (e.g., James et al., 2019; Westoby et al., 2012; Dering et al., 2019). SfM photogrammetry provides a means to digitally preserve outcrops and generate outcrop-truthed, georeferenced spatial data as digital outcrop models (DOMs) (Westoby et al., 2012; Burnham et al., 2022).

Outcrop analogue studies have supported subsurface developments the petroleum industry and underground waste storage
35 (e.g., CO₂, nuclear waste, gas) for several decades (Howell et al., 2014; Marques et al., 2020). Subsurface data often suffer from non-uniqueness, i.e., loosely constrained solutions based on data that are often sparsely and unevenly distributed. In areas of good exposure, outcrop analogue studies provide high resolution data with significantly better spatial constraints and absolute spatial scales (Vollgger and Cruden, 2016). Outcrop-based mapping of stratigraphy and discontinuous structures like folds, faults, and fractures from cm to km scale is therefore pertinent to understanding geological processes, not least those
40 affecting storage and sealing capacity (e.g., Ogata et al., 2014, 2012; Sibson, 1996; Vollgger and Cruden, 2016). Through SfM photogrammetry, outcrops can be digitised to scale and geospatially referenced as DOMs to facilitate quantitative interpretation and integration with other spatial data sets (e.g., quantifying fracture orientation and spacing; (Senger et al., 2015)).

Extensive methodological reviews on the application of SfM photogrammetry are performed by, amongst others, Westoby et al. (2012), Smith et al. (2016), Dering et al. (2019) and James et al. (2019), often implementing unmanned aerial vehicles
45 (UAVs). SfM photogrammetry has been implemented to address a range of geomorphic (e.g., Leon et al., 2014; Rippin et al., 2015; Tonkin et al., 2016), sedimentary (e.g., Bilmes et al., 2019; Harrald et al., 2021) and structural questions (e.g., Mulrooney et al., 2018; Vollgger and Cruden, 2016) - even on other planets (e.g., Barnes et al., 2018).

Despite the increased implementation of DOMs, most data and interpretations remain inaccessible (Vieira et al., 2021; Burnham et al., 2022). Few repositories, such as V3Geo (Buckley et al., 2022) and e-Rock (Cawood and Bond, 2019) enable
50 the sharing of DOMs, yet do not openly share the input data (e.g., photographs) and processing parameters. Open-accessibility is essential for the reproducibility and re-evaluation of existing work, the application of new methodologies, and future studies of temporal processes (e.g., weathering and climatic variation). In addition to being openly available, the data (including input and processing parameters) must be of high quality and properly documented (Burnham et al., 2022).



In this contribution we present the acquisition, processing and integration of the Konusdalen West digital model data set, including a high-resolution, georeferenced DOM and orthomosaics covering the faulted, mudstone-dominated Agardhfjellet Formation in Svalbard, Arctic Norway.

1.1 The study area and outcrop geology

The High Arctic archipelago of Svalbard (Fig. 1) is part of the uplifted north-western margin on the Barents Shelf (Henriksen et al., 2011). The outcropping strata range from the Archean to Quaternary in age and offer a wide range of lithologies and tectonic settings. The strata in Svalbard have been shaped by several orogenic events, including the West Spitsbergen Fold and Thrust Belt (WSFTB) in the Palaeogene. Early Cretaceous magmatism introduced a system of dykes and sills as well as lava flows into the stratigraphy, whilst glaciations and periglacial events over the last 100 ka have shaped the present-day landscape and modern exposure patterns (Harland et al., 1997; Henriksen et al., 2011; Senger et al., 2014). Following the last ice age, approximately two-thirds of the archipelago remains covered by glaciers, with the remainder affected by periglacial processes, permafrost and featuring almost no vegetation (Humlum et al., 2003).

Petroleum and coal exploration boreholes have contributed significantly to our understanding of the stratigraphic evolution of both Svalbard and the greater Barents Shelf (Senger et al., 2019). The Longyearbyen CO₂ Lab drilled eight fully cored wells in central Spitsbergen to assess a heavily fractured Mesozoic reservoir and caprock, comprising the Wilhelmøya Subgroup and Janusfjellet Subgroup, respectively. The drilling provided wireline, stratigraphic, petrophysical, geophysical, and geochemistry data (Olaussen et al., 2019, and references therein), yet current top seal integrity remains difficult to ascertain with borehole data alone (Birchall et al., 2020; Huq et al., 2017). Geological constraints and inputs are needed to ascertain what may happen following injection, with the Konusdalen West outcrop ideally suited to investigate the role of faults and fractures in mudstone-dominated sequences (e.g., Ogata et al., 2012), as it covers the lower part of the caprock.

The fractured reservoir sections targeted by the Longyearbyen CO₂ Lab belong to the Upper Triassic to Middle Jurassic Kapp Toscana Group. The sandstone-dominated De Geerdalen Formation and overlying Wilhelmøya Subgroup represent paralic and deltaic depositions, respectively (Mulrooney et al., 2018). These are overlain by 450 m-thick, regional, shale-dominated caprock succession belonging to the Janusfjellet Subgroup (Koevoets et al., 2019; Braathen et al., 2012; Olaussen et al., 2019). The Janusfjellet Subgroup comprises the Late Jurassic-Early Cretaceous Agardhfjellet and Early Cretaceous Rurikfjellet formations (Collignon and Hammer, 2012; Dypvik et al., 1991; Grundvåg et al., 2017; Mørk et al., 1999; Koevoets et al., 2019).

The Agardhfjellet Formation was formed mostly under dysoxic to anoxic conditions, periodically experiencing oxygenation of the water column (Collignon and Hammer, 2012). It forms the caprock immediately overlying the targeted reservoir of the Longyearbyen CO₂ Lab and crops out at Deltanaset, some 15 km north-west of Longyearbyen (Fig. 1) (Braathen et al., 2012; Olaussen et al., 2019). Time-equivalent stratigraphic intervals of the Agardhfjellet Formation are widespread across the Barents Sea and are prolific regional source rocks, in addition to being the top seal of several oil and gas fields on the Norwegian continental shelf (e.g., Spencer et al., 2008).

Within our study area, the Agardhfjellet Formation is up to 250 m thick and can be subdivided into four member units (Dypvik et al., 1991; Koevoets et al., 2018, 2019). The Oppdalen Member is a fining-upward unit of Bathonian-Oxfordian

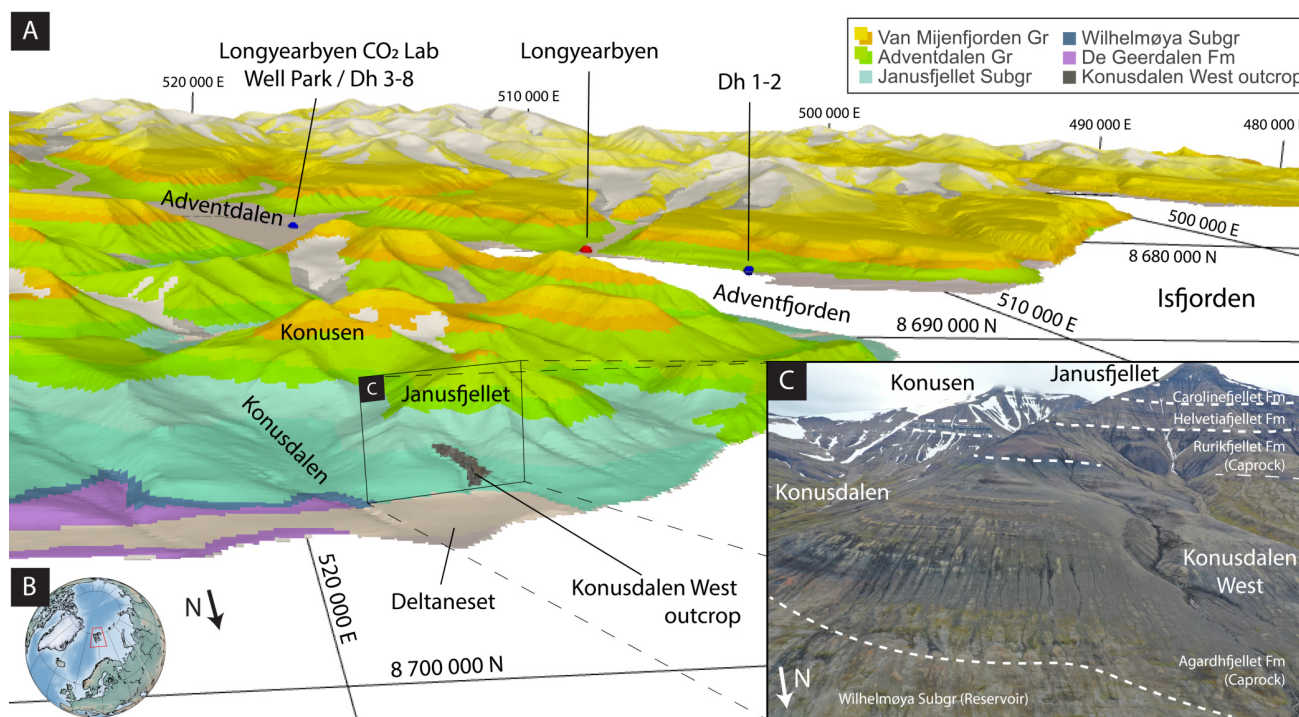


Figure 1. Location and geology of the Longyearbyen CO₂ Lab reservoir, caprock and overburden successions in Svalbard (B). The locations of the outcropping Konusdalen West exposures at Deltaneset, the city of Longyearbyen, and both drill sites of the Longyearbyen CO₂ Lab are highlighted. The inset (C) shows an overview photo of the study area. Geological map (1:250 000) and digital terrain model (50 m resolution) are courtesy of Norwegian Polar Institute (2014) and Norwegian Polar Institute (2016).

age, deposited in a shallow-marine environment. The Lardyfjellet Member overlies the Oppdalen Member and consists of black paper shales with scattered carbonate concretions. The first appearance of silt-sand beds and disappearance of black shales marks the transition into the Oppdalssåta Member. The Upper Kimmeridgian Oppdalssåta Member comprises several upward-coarsening sandstone and sandy shale units, of which the last marks the end of the member. The Slottsmøya Member (Lower Volgian–Ryazanian) consists of black paper shales, developing slightly coarsening-upwards sequences in the upper part.

Considerable lateral variation of the formation is observed throughout Spitsbergen, both in total thickness and in the relative thicknesses of its members. Tectonic disturbances of the mechanically weak Agardhfjellet Formation are likely to have occurred through the WSFTB (Braathen et al., 1995; Bergh et al., 1997). The Paleocene-Eocene evolution of the WSFTB resulted in a series of eastward-transported thrust sheets rooted in sub-horizontal decollement zones along weaker evaporite and shale intervals, including the Agardhfjellet and Rurikfjellet formations (Ogata et al., 2012).



The Rurikfjellet Formation features several coarsening-upward units, deposited in a marine shelf to prodeltaic and shoreline
100 delta-front environment (Dypvik et al., 1991; Grundvåg et al., 2017). Transition from the Agardhfjellet Formation into the
Rurikfjellet Formation is marked by the Myklegardfjellet Bed, a distinct and easily observable clay unit (Dypvik et al., 1991).

2 Methods

2.1 UAV surveying

UAV-based acquisition of the outcrop was conducted over two weeks in July and August 2020. We used a DJI Mavic 2 Pro
105 drone with a Hasselblad L1D-20c camera (10.26 mm focal length; 20 MP images) with built-in GNSS positioning to image
the Konusdalen West outcrop at an average distance of 35.2 m. Maximum flight velocity was kept at 1.1 m s^{-1} with image
acquisition triggered automatically at 5 second intervals and resulting in 5512 images (Fig. 2, Table A1).

2.2 Ground control points and structural location measurements

Fifteen control points were laid out around the eastern slope of the best-exposed part of the Konusdalen West outcrop (Fig. 2).
110 Control point locations were measured prior to the UAV survey in August 2020 using a LEICA Viva GS16 receiver with
LEIGS antenna (pole length: 1.800 m). Each location was measured for at least 30 seconds and calibrated against the long
observation base station in Longyearbyen (“LYRS”; TRIMBLE NETR9 receiver with TRM41249.00 antenna), approximately
15 km south-west of the study area ($78^{\circ} 13' 43.77'' \text{ N}$, $15^{\circ} 23' 50.32'' \text{ E}$, and 495.682 m WGS84 ellipsoidal height; 509048.1382
E, 8683937.5685 N, and 463.4025 m orthogonal height [WGS84/UTM Zone 33N with Earth Gravitational Model 2008,
115 EGM2008]) using a post-processing static approach. Post-processing performance of the Leica Viva GS16 system is rated
at $3 \text{ mm} + 0.1 \text{ ppm}$ horizontal and $3.5 \text{ mm} + 0.4 \text{ ppm}$ vertical accuracy (Leica Geosystems AG). This translates to an overall
accuracy at the targeted field site of $\pm 1.8 \text{ mm}$ horizontally and $\pm 9.5 \text{ mm}$ vertically. One-second interval base station data
were retrieved through ftp.statkart.no in the RNX2 and RNX3 formats. The Leica Infinity software package (v3.6.0.35318;
64bit) was used for processing, implementing EGM2008 (Pavlis et al., 2008) for the calculation of orthogonal heights from
120 the measured WGS84 ellipsoidal heights. In accordance with the guidelines proposed by Dering et al. (2019) and James et al.
(2019), ten markers were used as ground control points (GCPs) for calibration of the point cloud. The remaining five were used
as check points (CPs).

The use of ArUcO markers enabled the automated analysis and control point-detection in the images by using the OpenCV
ArUcO library (Bradski, 2000; Garrido-Jurado et al., 2014). The automated_metashape package (v1.1.10, Betlem, 2022a)
125 streamlined the integration thereof with Agisoft Metashape through use of the Metashape Python API. The ArUcO markers
implemented the DICT_6X6_250 encoding. Each automated control point marker placement was subsequently checked and
where needed manually refined to ensure the highest precision and accuracy.

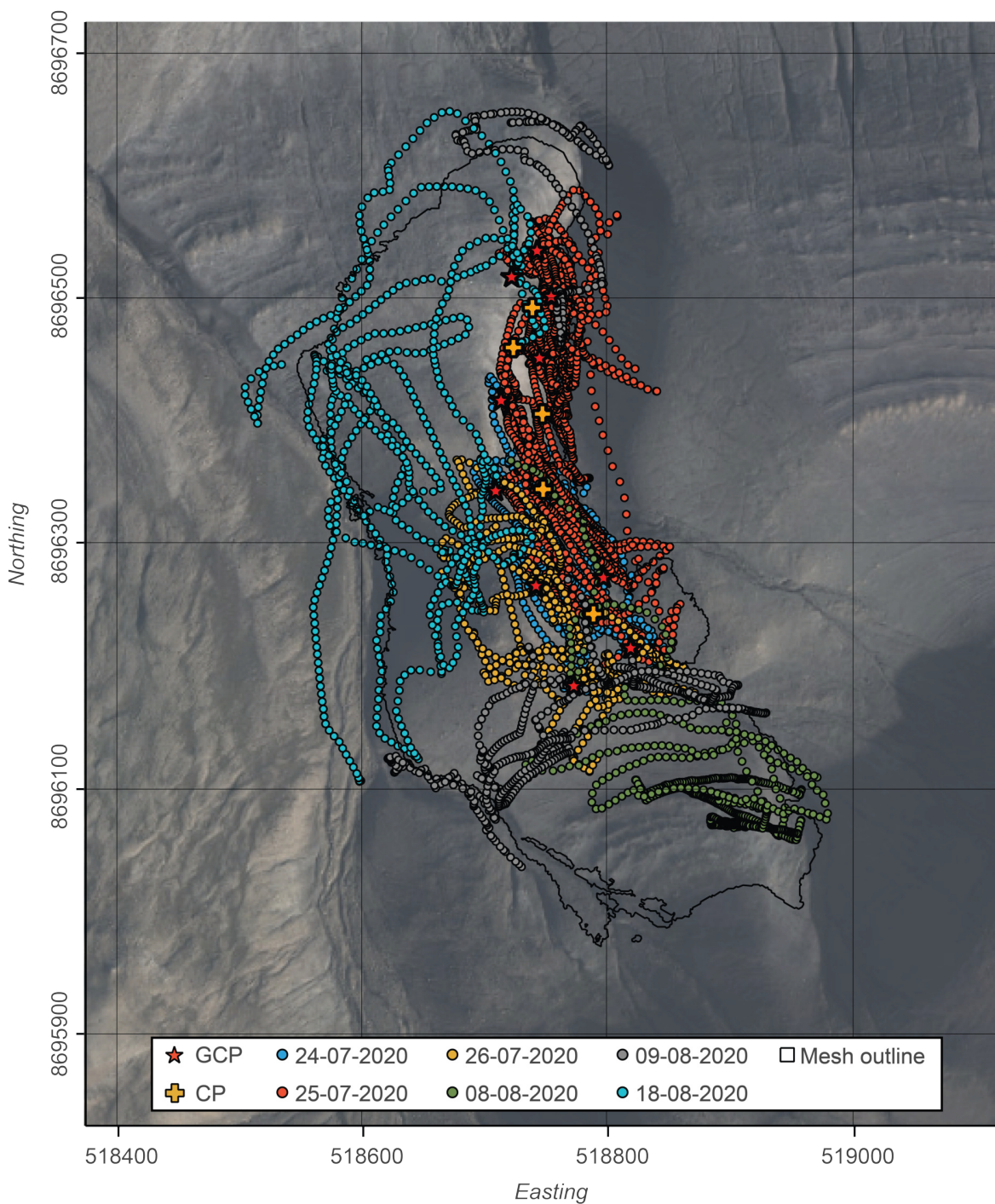


Figure 2. Targeted area and control point and image acquisition locations. Images are grouped by acquisition date. GCP: ground control point; CP: check point. Background orthophoto is courtesy of Norwegian Polar Institute (2017). Map uses the WGS 84/UTM zone 33N (EPSG:32633) projection.



We measured additional fault and fracture orientation data by handheld-compass in June 2021. The measurements followed excavation of up to half a metre of material and were located with the Leica Viva GS16 system. The structural measurements supplement and constrain digital annotations and provide additional surface elevation reference data.

All recorded coordinates are provided in Table 1 and Table C1, including model errors, using the WGS84/UTM Zone 33N coordinate system (EPSG:32633) and orthogonal heights (altitudes) derived from EGM2008 (Pavlis et al., 2008).

2.3 Point cloud, orthophoto mosaic and digital outcrop models

Image processing and surface reconstruction were performed using Agisoft Metashape (formerly PhotoScan, v1.7.2.12040). Metashape is a commercial software that implements automatic feature detection, image matching and modelling using SfM algorithms, and is frequently used for model reconstruction (e.g., Tinkham and Swayze, 2021; Zhou et al., 2020; Kingsland, 2020). Agisoft does not disclose the exact algorithms used in the processing, but does refer to Hirschmuller (2007) and Hiep et al. (2009).

Processing was performed in local area network (LAN)-mode on six dedicated workstations (Table B1) and proceeded according to the latest USGS coastal imagery processing guidelines (Over et al., 2021). For a schematic summary of the steps involved, the reader is referred to Fig. 1 in Over et al. (2021). Minor deviations from the workflow and processing parameters are discussed below.

We quality controlled all images prior to processing and additionally used Metashape's inbuilt image assessing tool to quantify image quality. Four images did not pass the specified cutoff of 0.5 and were disabled. Image location metadata for flight 23-25 featured erroneous altitude data in excess of 100 m above the recorded flight paths. Location metadata for these images ($n = 748$) were disabled prior to the photo alignment step. The sparse point cloud was generated using the highest setting (i.e., four times upscaled image) through two consecutive iterations to re-align any non-aligned images, leaving four unaligned. Subsequent camera optimization only utilized the high-precision GCP data, disabling all image location metadata and unpinned (implicit, "blue flags") GCP points to ensure the most accurate georeferencing. Tie points were filtered on reconstruction uncertainty (level = 15, one optimization, removed 16 021 109 points, disabled four cameras), projection accuracy (level = 2, one optimization, removed 2 497 962 points, disabled three cameras) and reprojection error (level = 0.3, seven optimizations, removed 4 650 001 points, disabled two cameras). A camera alignment-optimization step followed each filtering step. The depth maps and dense point cloud were processed using the half-image scale and applied "mild" filtering of the generated depth maps. No changes were made to the automatically-generated bounding box.

The dense cloud was trimmed based on confidence (retaining $10\leq$ point confidence, removed 1 034 950 382 points) to improve overall quality. The trimmed dense cloud featured as input for the generation of a (textured) mesh, tiled model, and digital terrain model (DTM). Contours were extracted from the DTM at 5 m steps across the 85-255 m interval. The mesh and DTM were used for the generation of several orthomosaics, including top-down and viewpoints aligned with the key geological features of interest. A processing report detailing additional processing parameters is made available as part of the data set (Betlem, 2022b).



2.4 Point cloud, vertex and data operations

We analysed point cloud and mesh data using Python's Point Data Abstraction Library, PDAL (PDAL Contributors, 2018; Butler et al., 2021, v. 2.2.0/2.4.2 (python-pdal)). Point cloud data were exported as single .LAS files, while mesh data was PDAL-converted from the .obj file format to the .LAS file format. Point cloud and mesh data were subsequently split into one
165 m² bins from the (500000, 8680000) grid origin using the PDAL-splitter filter. Points per bin, extent, and bin centres were calculated for both tie points and dense cloud data. Mean confidence was additionally calculated for each m² binned interval. Outlines were calculated with PDAL's hexbin filter, specifying an *edge_length* of 0.6204 units (m). Slopes and aspects were calculated from the DTM data through use of OSGeo and GDAL/OGR (Rouault et al., 2022, v. 3.2.1). Functional scripting examples are found in the digital appendix, and include point and vertex density, boundary estimate, and error calculations.

170 2.5 Delineation and structural measurements of geological features in the point cloud and digital terrain models

Metre-scale geological features were interpreted as georeferenced 3D features on the dense point cloud, textured mesh and tiled model through use of Metashape's built-in polygon tool. Published sedimentary logs (Koevoets et al., 2018, 2016) helped with the integration of the model into its geological context and aided the placement of formation and member boundaries. Marker beds and faults were traced only where clearly visible along the entire DOM and confirmed in the field.

175 2.6 Accuracy assessment and mis-alignment

Accuracy assessment implemented the error associated with the geometric accuracy of the dense cloud and digital terrain model (DTM). We calculated mean and Root-mean-square errors (RMSE) for both the GCPs and CPs and employed differential augmentation of the global navigation satellite system (dGNSS) to constrain the lateral and vertical accuracy of the DTM at the control points. The altitude-DTM difference was in addition calculated for dGNSS data recorded for structural measurements
180 and against available 5 m-resolution DTM reference data (Norwegian Polar Institute, 2014).

2.7 Visualisation and data integration

We employed the WGS 84/UTM zone 33N (EPSG:32633) projection. The Norwegian Polar Institute provided geological maps with 1:250 000 and 1:100 000 scales (Norwegian Polar Institute, 2016). We used Python's Bokeh, HoloViews (Stevens et al., 2015) and Scientific colour maps 7.0 (Crameri et al., 2020) libraries for the visualisation of the data as georeferenced
185 maps. Given computational and file-size limitations, the DTM, aspect, slope, and orthomosaic data were downsampled prior to visualisation. In line with file-size limitations and publishing policy, a decimated copy of the textured mesh (5 M faces) was filtered on connected component size (99%) prior to submission to V3Geo and SketchFab.



3 Results and Discussion

3.1 Point clouds and control points

190 The initial tie point set (i.e., sparse cloud) consists of 29 492 561 points following camera alignment, trimmed to 6 323 579
points through error-reducing camera optimization steps (Fig. 3). Tie point multiplicity, i.e., the average number of images
where the point has been measured, of the processed point cloud is calculated as 3.81. The processed sparse cloud features an
RMSE reprojection error value of 0.12 pixels and a max reprojection error of 0.88 pixels.

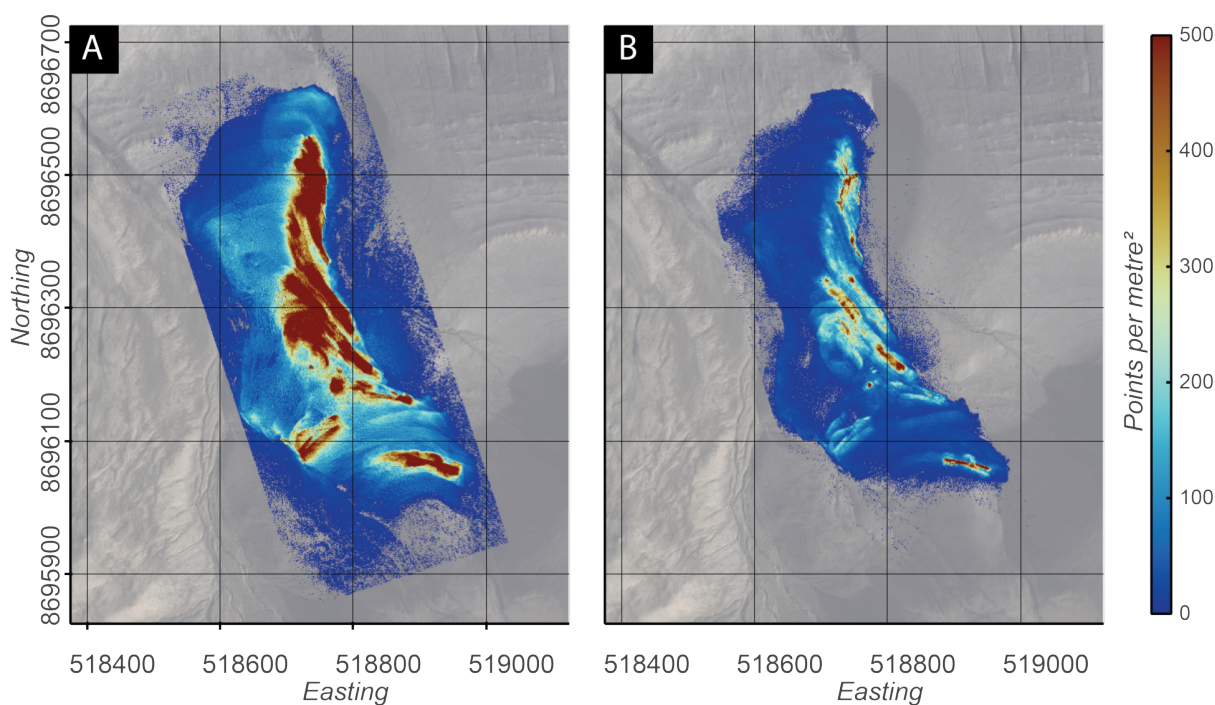


Figure 3. Sparse cloud point density maps, featuring both the raw tie point set (A) and the optimized point cloud (B). Highest point densities are found close to control points and steeper sections. Maps use EPSG projection 32633. Orthophoto courtesy of Norwegian Polar Institute (2017).

195 The full-extent dense point cloud (Fig. 4) consists of 1 543 094 332 points and features a median point-to-point distance of
1.26 cm and 6222 points m^{-2} density (std. dev. of 4767 points m^{-2}), covering a total area of 0.245 km^2 . Full-extent dense cloud
confidence ranges from 1 to 119.5, with confidence values above 9 considered high.

200 Point exclusion of low-confidence points led to an improvement in mean confidence from 10.24 to 29.43 for the reduced
dense cloud (508 143 950 points), mainly through the removal of points closer to the edges of the surveyed area (Fig. 4). The
filtered dense cloud has a median point-to-point distance of 1.57 cm and features an average point density of 3824.9 points m^{-2}
(std. dev. of 2215.4 points m^{-2}).

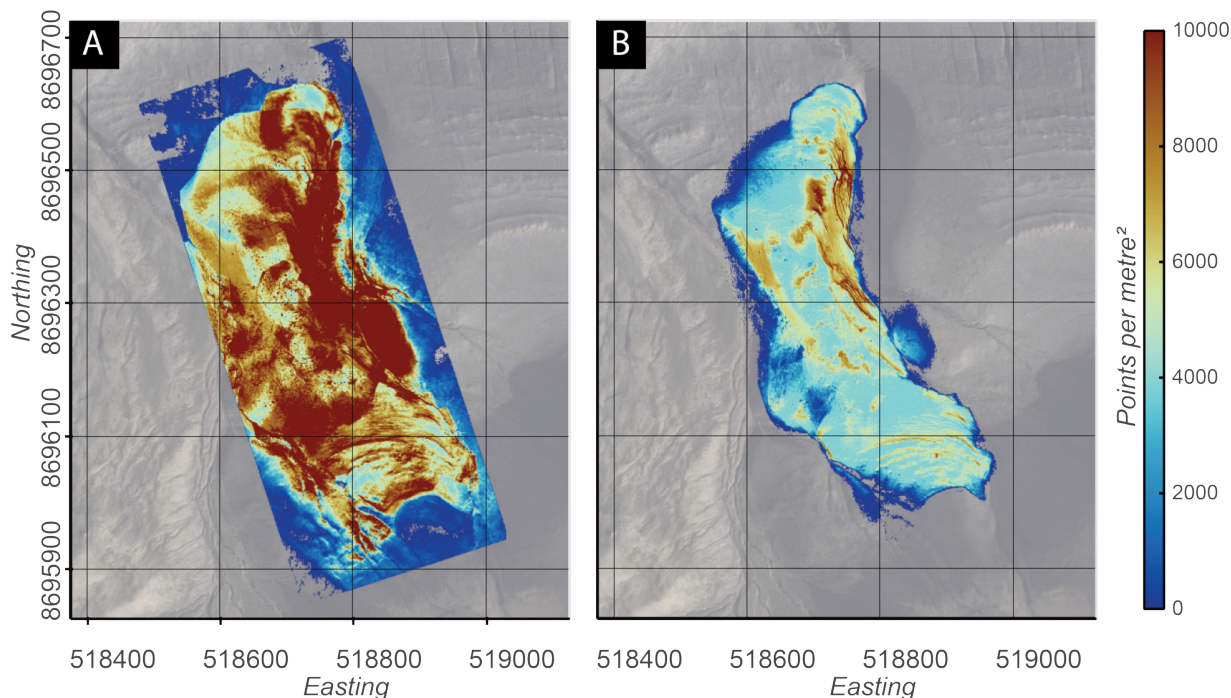


Figure 4. Dense cloud point density maps, featuring both the raw point set (A) and the confidence-filtered point cloud (B). Highest densities are found close to control points and steeper sections. Maps use EPSG projection 32633. Orthophoto courtesy of Norwegian Polar Institute (2017).

The spatial accuracy of the point cloud was assessed using five independent CPs, disabled during point cloud generation and camera optimization (Table 1). All GCPs and CPs besides GCP 15 and CP 02 featured a post-processed phase fixed point solution, i.e., *Fixed PP*. Post-processing of GCP 15 and CP 02 resulted in less accurate code solutions, i.e., *Code PP*. Overall CP RMSE is 1.95 cm in X, 1.33 cm in Y and 5.17 cm in Z, with the overall XYZ error calculated at 5.69 cm. Slightly larger errors were observed for the GCPs (Table 1). Overall GCP RMSE of the ten points is 2.95 cm in X, 6.39 cm in Y and 21.80 cm in Z, with the overall XYZ error at 22.90 cm. Removal of 3-sigma outliers, i.e., GCP 2, lowered the RMSE to 9.8 cm, bringing the calculated errors in line with the RMSE XYZ error calculated for the CPs.

Table 1: Ground control points (GCPs) and Check points (CPs) used for high-resolution georeferencing. Easting and Northing given in the epsg:32633 reference system. Heights are the calculated ortho heights using Earth Gravitational Model 2008 (Pavlis et al., 2008).

Marker	Type	Images	Northing (y, m)	Easting (x, m)	Altitude (m)	Error (x, m)	Error (y, m)	Error (z, m)	Error (xyz, m)	DTM (m)	Alt.-DTM (m)
01	GCP	89.0	8696183.479	518772.856	192.404	0.062	0.016	0.008	0.065	192.417	-0.014
02	GCP	115.0	8696265.172	518742.048	188.769	0.018	-0.057	-0.660	0.662	188.103	0.666
03	GCP	88.0	8696342.463	518709.156	170.5	-0.000	-0.004	-0.003	0.005	170.503	-0.003
04	GCP	58.0	8696416.147	518713.526	151.964	-0.016	-0.004	-0.014	0.022	151.953	0.011
07	GCP	70.0	8696450.708	518744.881	120.22	0.001	0.010	-0.022	0.024	120.195	0.024
10	GCP	61.0	8696516.925	518722.178	129.467	-0.001	0.002	0.033	0.033	129.544	-0.077
11	GCP	60.0	8696538.309	518742.953	108.885	0.003	0.005	-0.045	0.046	108.851	0.034
12	GCP	74.0	8696500.905	518754.466	104.902	0.001	-0.008	-0.002	0.008	104.9	0.001
14	GCP	48.0	8696271.709	518797.111	163.658	-0.002	0.003	-0.018	0.018	163.633	0.026



Marker	Type	Images	Northing (y, m)	Easting (x, m)	Altitude (m)	Error (x, m)	Error (y, m)	Error (z, m)	Error (xyz, m)	DTM (m)	Alt.-DTM (m)
15	GCP	83.0	8696214.39	518819.154	180.902	0.068	-0.192	0.188	0.277	181.002	-0.100
Mean	GCP	74.6	-	-	-	0.013	-0.023	-0.053	0.116	-	0.057
Mean (excl. GCP 02)	GCP	70.111	-	-	-	0.013	-0.019	0.014	0.055	-	-0.011
RMSE	GCP	-	-	-	-	0.030	0.064	0.218	0.229	-	0.215
RMSE (excl. GCP 02)	GCP	-	-	-	-	0.031	0.064	0.066	0.098	-	0.046
05	CP	104.0	8696343.978	518747.921	151.448	-0.034	0.021	0.036	0.054	151.485	-0.037
06	CP	68.0	8696405.441	518747.357	131.928	0.019	-0.003	-0.054	0.058	131.888	0.040
08	CP	113.0	8696459.538	518723.651	137.547	-0.005	0.018	0.053	0.056	137.603	-0.055
09	CP	81.0	8696492.032	518739.179	129.011	-0.005	-0.004	-0.011	0.013	128.996	0.015
13	CP	56.0	8696242.35	518788.954	178.719	0.018	0.010	-0.079	0.081	178.658	0.061
Mean	CP	84.4	-	-	-	-0.001	0.008	-0.011	0.052	-	0.005
RMSE	CP	-	-	-	-	0.020	0.013	0.052	0.057	-	0.045

The sparse and dense point clouds featured very high point densities near control points and across steeper terrain intervals. Both are partly biased by the here-employed sampling and processing methods. Control points feature increased point densities as additional photographs were taken to streamline and improve automated-marker detection, i.e., sampling bias. The reported two-dimensional point densities do not properly account for three-dimensional variations, with vertical features condensed into two-dimensional representations. Neither, however, affect the quality of the model following the confidence-enhancing processing steps. Areas further away from the best-exposed, eastern slope of the Konusdalen West outcrop generally featured lower point densities. The southernmost part, for example, features a lower imaging-density than the densely photographed eastern side (Fig. 2). The density-drop in the south-west is similarly caused by a lower imaging-density. Decreased point densities were also observed on the shadow sides of obscuring features. Overall camera obscurement, however, remained minimal, being very localised and often smaller than 0.25 m² and well below the 1 m² area used for binned interval calculations shown in Fig. 3 and Fig. 4. The occurrence of rocks and boulders provides additional data on the composition and mechanical stability of the slope. Such data may also be of use to researchers from other disciplines enabling better integration of future multi-disciplinary workflows.

3.2 Digital terrain model, outcrop model, and orthomosaics

The textured mesh features a mean vertex density of 395.29 vertices m⁻², a factor of 10 lower than recorded for the dense cloud and covers an area of 0.12 km² (Fig. 5). Vertex density ranges from 1 to 3458 vert. m⁻² (std. dev. 150.89 vert. m⁻²), with higher values observed in parts corresponding to steeper sections and more competent lithologies with higher quartz content. Vertex density and resolution are more than sufficient for digital annotation and quantitative measurements of the outcrop.

Interpolation of the dense cloud enabled the generation of a DTM (Fig. 6) with a 1.6 cm/pixel resolution. The DTM features a range in elevation from 84.36 m to 256.23 m. For evaluating the elevation accuracy of the DTM, elevations were compared with the GPCs/GCs, structural measurement locations obtained by dGNSS (Table 1), and existing DTM data available from the Norwegian Polar Institute (Norwegian Polar Institute, 2014). Point altitude/elevation differences range from -4.77 cm to 100.39 cm (18.99 cm, excluding outliers) for the GCPs and -10.60 cm to 8.62 cm for the CPs. GCPs feature a mean altitude-elevation

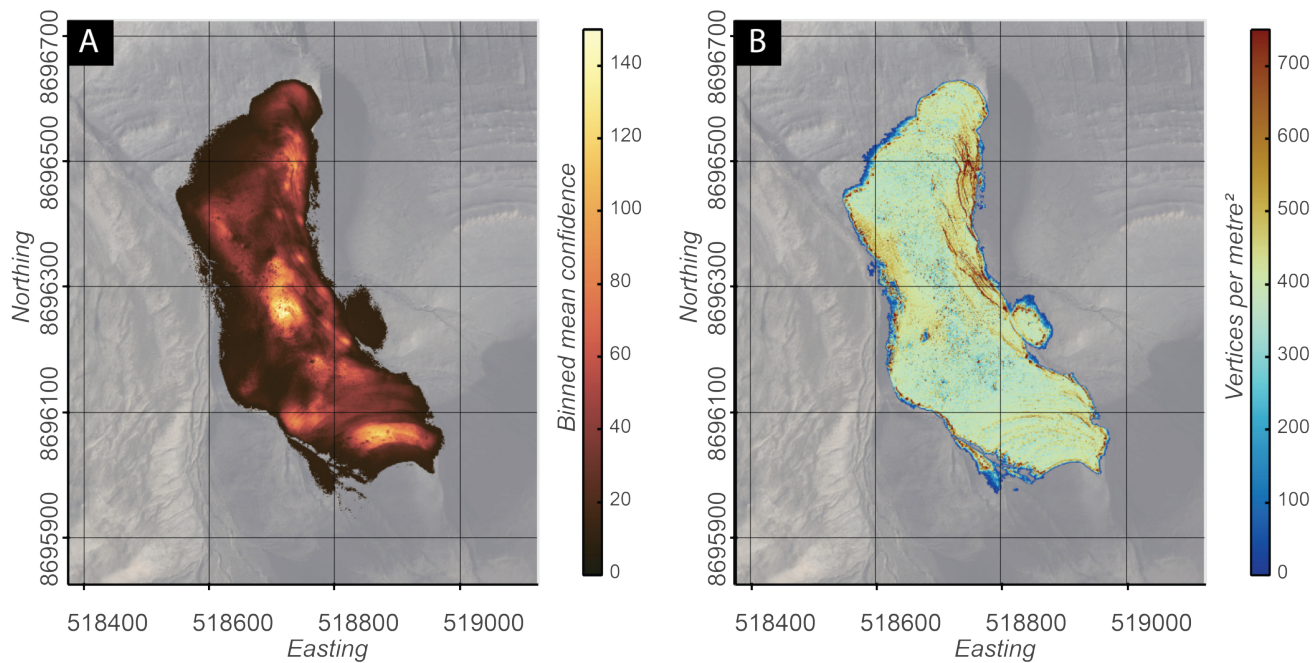


Figure 5. Dense cloud point confidence and mesh vertex density maps. The high-confidence dense cloud (A) was used as input for generation of the mesh (B) and other products. Maps use EPSG projection 32633. Orthophoto courtesy of Norwegian Polar Institute (2017).

error and RMSE of 11.84 (1.89) cm and 32.75 (7.10) cm, respectively, when compared to the DTM, with the error in brackets stemming from outlier removal. CPs feature a mean altitude-elevation error and RMSE of -1.47 cm and 7.27 cm, respectively.

An additional 72 points were measured to constrain fault locations and orientations in the outcrop, so-called ground-truthing points (Table C1; Fig. 2). Post-processing of the points led to 19 *Code PP*, 17 *Widelane PP*, and 36 *Fixed PP* solutions, with
235 *Widelane PP* being slightly less accurate than *Fixed PP* solutions (Table C1). Altitude comparison with the DTM yields mean errors of between 1.2 cm and 16.6 cm. Accompanying RMSE errors show a larger spread, ranging from 1.369 m for *Code PP* to 22 cm for *Fixed PP* solutions. As also for the control points, errors are largest in the lowermost part of the outcrop close to the stream, where GNSS coverage is affected by horizon obstruction in the gully. The ground-truthing points show larger
240 errors than those recorded for the GCPs/CPs. Measured a year after the UAV survey, the error-difference may be indicative of geological processes (e.g., active layer freeze-thaw) acting on the outcrop, as also evidenced from the comparison with the published 5 m-resolution DTM reference (Norwegian Polar Institute, 2014).

The Konusdalen West DTM differs on average by +0.927 m from the reference (Fig. 6). The largest positive deviations (<5.11 m) are observed along the steepest section at the outcrop's eastern side. A few negative deviations (>-0.73 m) are found towards the west. The differences fall within the 2 to 5 m range listed for the standard deviation of the reference data set
245 (Norwegian Polar Institute, 2014) and suggest both DTMs are in agreement.

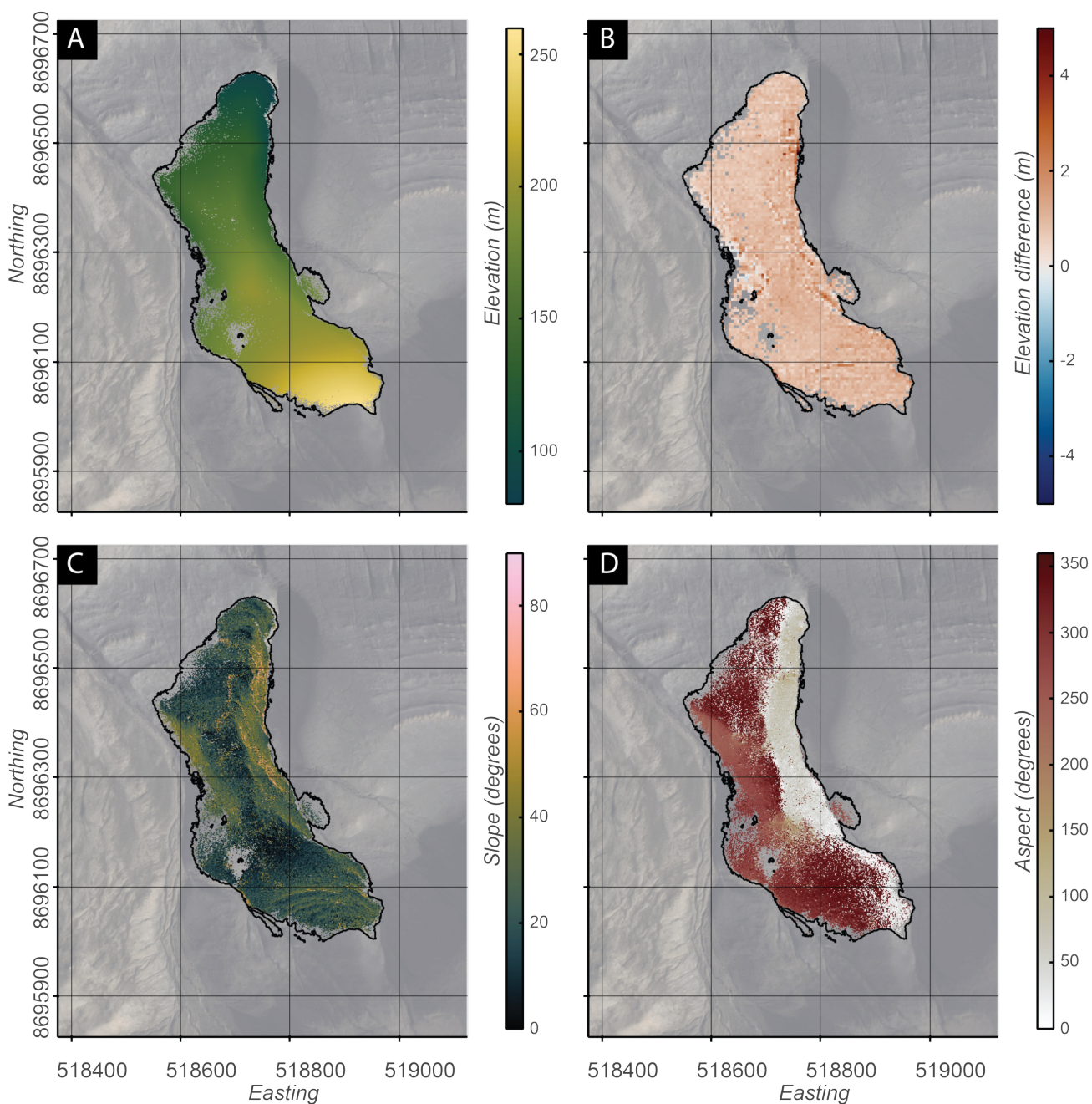


Figure 6. Digital Terrain Model (DTM) and related products. The difference between the Konusdalen West DTM and existing DTM reference data (Norwegian Polar Institute, 2014) is shown in B. Calculated slopes and aspect of the Konusdalen West exposure are shown in C and D, respectively. Maps use the WGS 84/UTM zone 33N (EPSG:32633) projection. Orthophoto courtesy of Norwegian Polar Institute (2017).



The DTM is of high enough quality for the generation of slope and aspect maps (Fig. 6) and high resolution orthomosaics. The latter (e.g., Fig. 7 B, Fig. 9) complement the data package with view-specific resolutions of up to 8 mm per pixel, which is twice as detailed as available for the DTM. Fig. 7 B depicts the highest resolution afforded by the data package. Fractures and other observations up to sub-cm scales can be identified and annotated as georeferenced features.

250 The outline of the DTM visualises minor gaps in the data sets, including lower data coverage toward the edges of the model. The presence of two larger, low-density areas is also marked in Fig. 7 by interior polygons and is a result of insufficient image coverage due to operator selection of better exposure and manually-operated UAV flights.

Topographic challenges and the remoteness of the site prevented the use of autonomous drone missions. Like most of Svalbard, the study area does not have telecommunication coverage, ruling out internet-supported, advanced flight planning 255 services. Offline solutions exist, but do not adjust the flight path to account for elevation changes and require high-resolution terrain models to be available. The outcrop covers approximately 170 m of elevation difference and features several near-vertical sections next to a narrow gully (Fig. 6), further complicating automation and consistency of image acquisition.

Few other low-confidence, low-point/vertex-density areas exist and are shared by all worked-up products, i.e. DTM, DOM, and orthomosaics. We deem these mainly a result of confidence-enhancing filtering steps that were applied to the tie points and 260 dense cloud, a necessity in the processing workflow to assure output accuracy.

Confidence and density remain highest in the area covered by GCPs/CPs, focused on by a higher proportion of flights. Even in areas affected by quality reductions, the data remain of sufficient quality for a quantitative assessment at lower resolutions, and inherently capture enough evidence for future users to have a realistic expectation of data availability.

4 Visualisation and integration

265 The high quality DOM data allow quantitative interpretation of the entire outcrop, including deciphering the sedimentological and structural evolution of the area. When combined with local geoscientific datasets and fault core architecture observations, the quantifiable data sets combine into a powerful tool that lends itself to detailed integrated studies of the outcrop.

4.1 Stratigraphic-structural integration

The Konusdalen West DOM spans the middle-upper successions of the Agardhfjellet Formation. The model covers the Slottsmøya, 270 Oppdalssåta and Lardyfjellet members and displays internal bed characteristics in detail, as highlighted by Fig. 7 and Fig. 9. The stratigraphic boundaries and structural features have all been annotated directly on the digital model data. The points, lines and polygons are generated as fully georeferenced 3D data and can be easily exported, visualised and processed by other toolsets. A brief geoscientific integration is provided by the discussion that follows, an important aspect to the applicability of the geospatial annotations and data sets.

275 The lower limit of the outcrop sits atop a thick, inconspicuous succession of black shales beyond the lower limits of the model. At the very base of the DOM, a glauconitic bed and limestone concretions mark the transition from the Lardyfjellet to the Oppdalssåta members. Only the uppermost 10 m of the Lardyfjellet Member's succession of dark shale, siderite horizons

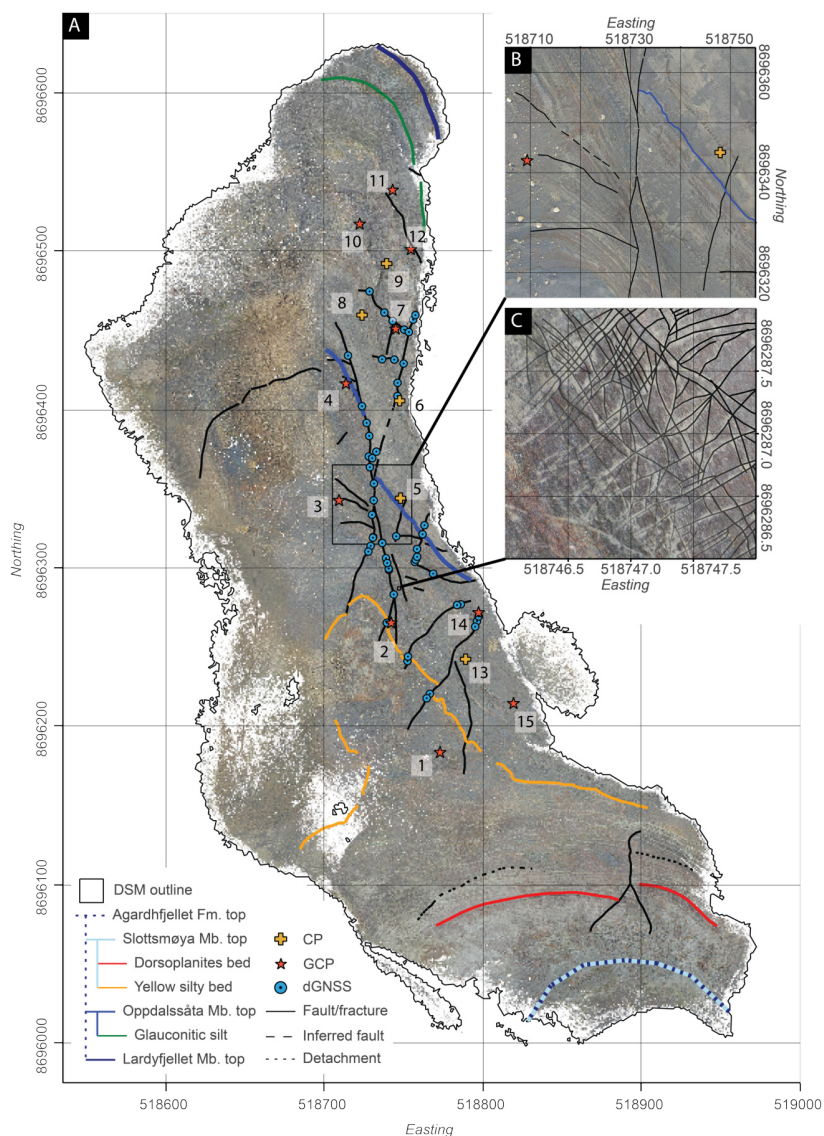


Figure 7. High resolution orthomosaics. A) Top-down view orthomosaic of the outcrop including control point locations and basic interpretations. Control points are subdivided into dGNSS points, ground control points, and check points. B) The 50-by-50 m zoom-in shows the lower part of the Slottsmøya member, including several annotated faults and marker beds. C) The orthomosaic is of high enough resolution to identify and delineate sub-cm scale features, as the fracture-mapped partial-overlay shows. Maps use the WGS 84/UTM zone 33N (EPSG:32633) projection.



and lenses are exposed and visible within the model (Dypvik et al., 1991; Mørk et al., 1999; Koevoets et al., 2018). The transition into the Oppdalssåta Member coincides with the start of a coarsening-upwards packages that span the lower half of the Konusdalen West outcrop. The coarsening-upwards shale, siltstone and sandstone packages come in 10 to 15 m-thick intervals. The member is considered to represent the coarsest grained interval of the Agardhfjellet Formation (Dypvik et al., 1991; Dypvik and Harris, 2001; Koevoets et al., 2018).

An approximately 10 m-thick black shale interval overlain by a 1 m-thick silty sandstone marks the transition into the Slottsmøya Member. The Slottsmøya Member consists of dark-gray to black-silty mudstone and discontinuous silty beds, including an abundance of siderite and dolomite interbeds and yellow-to-red sideritic concretions (Koevoets et al., 2018). The member can be separated into three parts, with their transitions demarcated by the Yellow Silty and Dorsoplanites Beds, both annotated in the Konusdalen West DOM and orthomosaics (Collignon and Hammer, 2012). The succession below the Yellow Silty Bed is dominated by siderite beds. The sequence above grades from a (paper) shale into a very-fine sandstone succession commonly abundant with ammonites, i.e., the Dorsoplanites Bed. The upper limit of the Konusdalen West DOM coincides with the Myklegardfjellet Bed and transition into the shales of the Rurikfjellet Formation.

Field and digital measurements identified at least two dozen, mainly northeast-southwest-trending normal and east-west antithetic faults within the Oppdalssåta and lower Slottsmøya members (Fig. 7 A, Fig. 9; Nakken (2020)). These orientations are consistent with faulting affecting the Wilhelmøya Subgroup reservoir and the Lardyfjellet and Oppdalen members of the Agardhfjellet Formation. Faulting in both sequences has been attributed to Palaeogene transpression during and following the evolution of the WSFTB (Mulrooney et al., 2018; Ogata et al., 2014). The Slottsmøya Member sequences up to the Dorsoplanites bed show evidence of strong shearing, exemplified by multiple detachment planes and numerous associated, steeply dipping thrust faults. The shear zone is a well-documented phenomenon in the upper Agardhfjellet and lower Rurikfjellet formations, one of two main detachment zones affecting the reservoir and caprock of the Longyearbyen CO₂ Lab targeted reservoir-caprock system (Ogata et al., 2014; Braathen et al., 1997; Bergh et al., 1997).

Exposed fault lengths vary between one metre and a few tens of metres, while offsets range from centimetre to decametre scale. Faults are generally disconnected, with the exception of a large, through-going fault that offsets a smaller, north-south striking fault by 8.5 m across the Oppdalssåta Member, Fig. 7 B. Continuation of the two faults into the lower half of the Slottsmøya Member is characterized by a splay-like structure that continues past the Yellow Silty Bed. Shallow excavation along the fault plane of the through-going fault provided insights to the thickness variations and heterogeneities within the fault core. Thickness increased with fault displacement and more competent host rock (up to 1.5 m). The fault core remained narrow (\varnothing : < 10 cm) within intervals dominated by black shales. The fault core architecture was dominated by network of anastomosing shale gouge membranes, intensely fractured shale lenses, and fault breccia, as seen in Fig. 8. Iron-cemented carbonate lenses were found in the lower-middle sequences of the Oppdalssåta Member, where such beds are abundant. The lenses are oriented in an elongate manner parallel to the fault axis and intensely fractured.

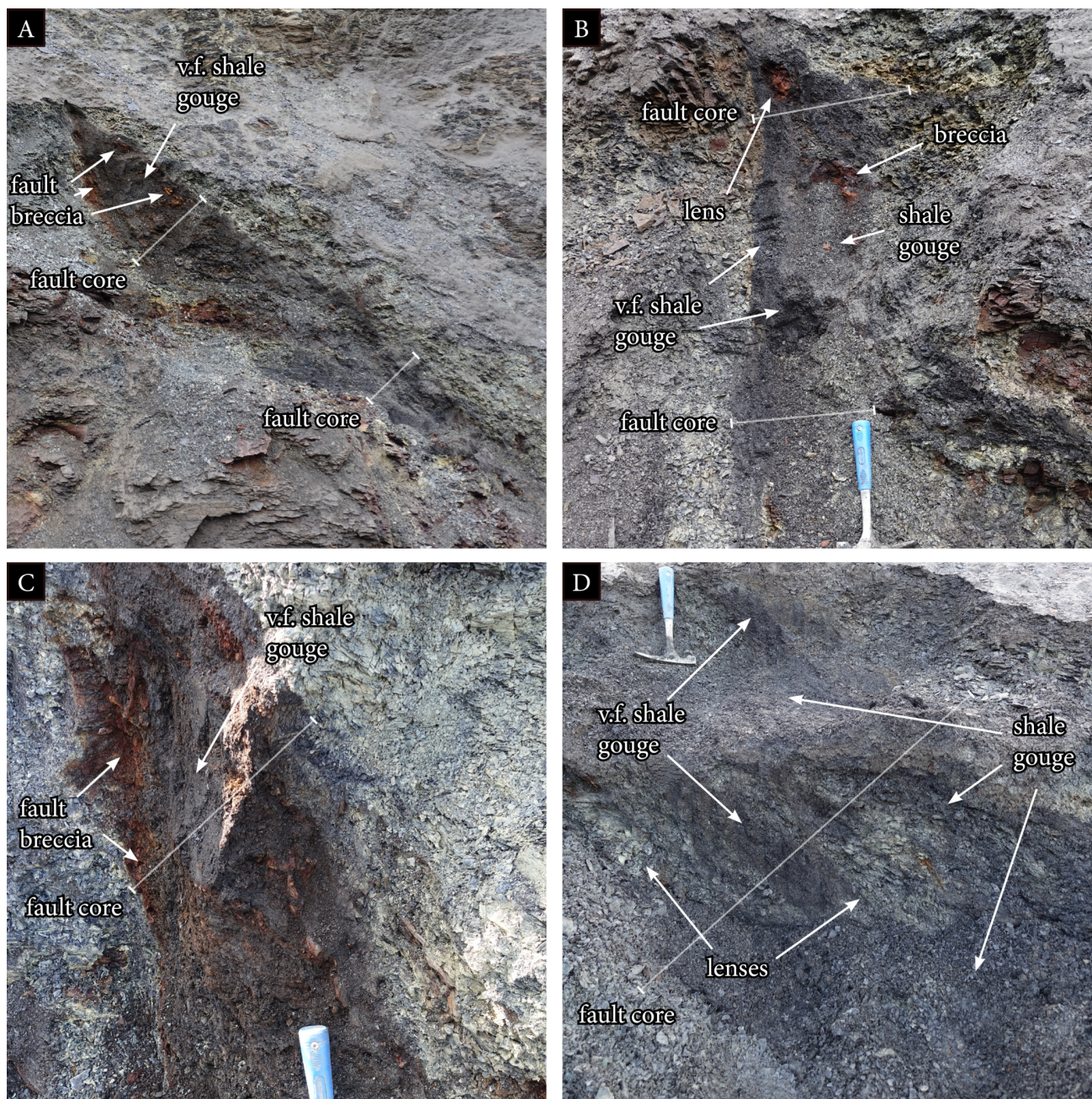


Figure 8. Fault core architectures at different points in the Konusdalen West outcrop. Fault core thickness varies depending on host rock lithology. Fault breccia and heavily fractured lenses are encompassed by fine to very fine shale membranes. Image locations are indicated in Fig. 9.

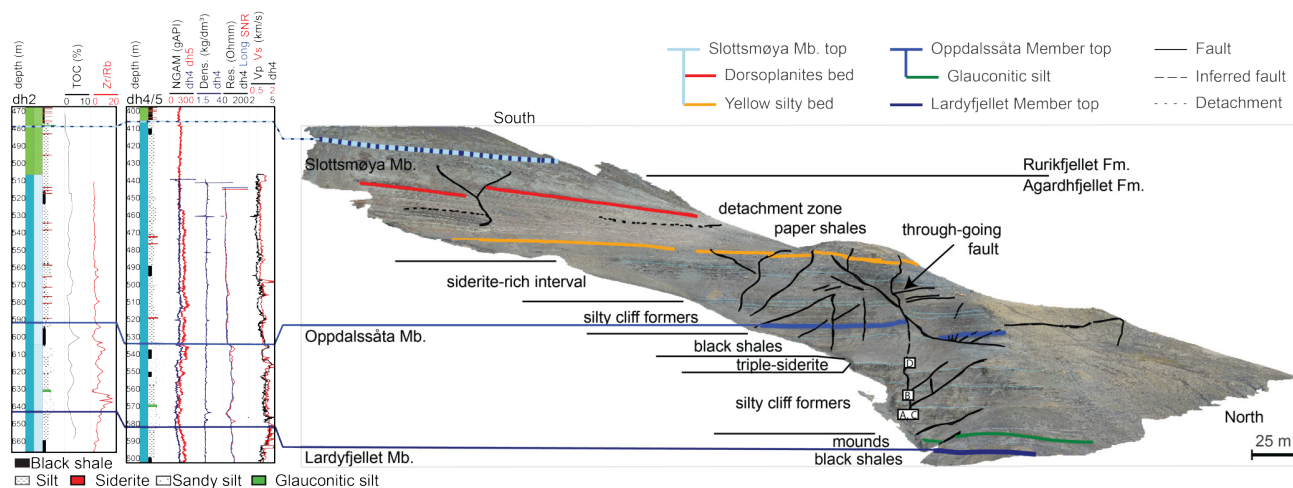


Figure 9. Side-view orthomosaic of the Konusdalen West DOM coupled with selected borehole data and borehole-outcrop integrations. Borehole data courtesy of the Longyearbyen CO₂ Lab, supplemented by data from Koevoets et al. (2018). A-D depict the locations of the images of Fig. 8.

310 4.2 The Longyearbyen CO₂ Lab borehole data

Provided with the stratigraphic correlation, the Konusdalen West DOM can be directly integrated with the Longyearbyen CO₂ Lab boreholes and drill core data (Fig. 9) (Schaaf et al., 2017; Nakken, 2020; Løvlie, 2020; Ogata et al., 2012, 2014). The digital and tiled models of the Konusdalen West outcrop are of high enough quality to map individual fractures with apertures smaller than 1 cm, as shown in Fig. 7 C. Open fractures and light-coloured, mineralized veins following lineaments are found throughout the digitised interval in three primary fracture sets, covering north-south, northeast-southwest and northwest-southeast striking orientations. Digital fracture tracing, Fig. 7 C, enables the quantification, validation and modelling of these networks (e.g., through FracPaQ; Healy et al., 2017; Rizzo et al., 2020, 2021), complementing the extensive set of available fracture data that cover both the outcrop (e.g., Løvlie, 2020; Nakken, 2020; Ogata et al., 2014) and drill cores from the fully cored caprock sequences (Ogata et al., 2014; Olaussen et al., 2019).

320 The Konusdalen West DOM and aforementioned correlations form an ideal starting point for a stratigraphic correlation at the bed-resolution that enable the generation of high-resolution, outcrop-truthed geomodels.

Populated with geochemical, petrophysical, geophysical, and wireline data (Olaussen et al., 2019, and references therein), the geomodels become suitable for numerical modelling, generate discretized fracture networks, assess fluid flow, and constrain the damage zone around faults. The Konusdalen West digital model data is thus key to appraisal of the caprock.



325 5 Data availability

The full Konusdalen West model, including input photographs, processing report, textured, tiled and surface models, can be freely downloaded from the Norwegian National Infrastructure for Research Data Research Data Archive (Norstore; <https://doi.org/10.11582/2022.00027>) (Betlem, 2022b). Visualisation and interpretation is possible through freeware (e.g., Agisoft's Viewer, Blender) and commercial software like LIME (Buckley et al., 2019). Reduced-size textured models and corresponding
330 metadata are available online through Svalbox (Senger et al., 2021), SketchFab, and V3Geo (Buckley et al., 2022), Table 2.

The full dataset (Betlem, 2022b) consists of the following files and zipped archives:

- A representative overview image file of the outcrop;
- Processing reports in PDF and HTML format;
- data.zip archive containing input UAV imagery, including disabled photos, and input differential GNSS data, including
335 GCP coordinates, field measurements and related errors;
- metashape.zip archive containing the Agisoft Metashape project featuring sparse and dense point clouds, mesh including textures, tiled model, DTM, and orthomosaics.
- export.zip archive containing exported DOM, DTM and orthomosaic data, as well as geopackages with delineation and structural measurements of geological features in epsg:32633 and local crs (epsg:4978).

340 The JupyterLab processing pages and examples have been uploaded to the Zenodo data repository under <https://doi.org/10.5281/zenodo.6497417> (Betlem, 2022c).

Table 2: Overview of available data.

Data set	Comments	DOI/URL/Reference
Input photographs, output (DTM, DOM, orthomosaic), processing report, Agisoft Metashape project, (interpretation) shapes	Data package	Betlem (2022b)
JupyterLab processing pages	Processing example package	Betlem (2022c)
Digital outcrop model and metadata	Svalbox digital model repository. In context with other Svalbard geoscientific data.	Svalbox ID: Svalbox-DOM_2020-0039
(Reduced component) digital outcrop model	SketchFab viewer. Web-based platform with virtual reality options.	SketchFab ID: 9d89ed14050c4498910dad86944bbdea
(Reduced component) digital outcrop model and metadata	V3Geo repository. Web-based platform with interpretation possibilities.	V3Geo ID: 391

6 Conclusion

We present high resolution digital models of the faulted, shale-dominated Agardhfjellet Formation caprock succession in Svalbard. The Konusdalen West digital outcrop model (DOM) has been ground-truthed via dGNSS and has been processed
345 according to community standards to improve confidence and reduce errors. The digital models feature maximum resolutions of 8 mm per pixel and outlier-removed, overall spatial accuracies of less than 10 cm. The (textured) surface models and orthomosaics enable the deciphering of the sedimentological and structural evolution of the area, including the delineation of



sub-cm scale features such as fractures. Areas of reduced quality stem mainly from operator selection of better exposures, i.e., the eastern and best-exposed part of the outcrop, and confidence-increasing processing. The quality of the otherwise pristine, faulted, mudstone-dominated outcrop is not affected. Further, the data captures the presence of obscuring features in high detail, which can be used to help constrain the composition and mechanical stability of the slope. The Konusdalen West model is suitable input for accurate, high resolution fracture mapping and geomodelling, especially when combined with available regional and Longyearbyen CO₂ Lab data sets. As time-equivalent stratigraphic intervals of the Konusdalen West outcrop are prolific regional source and caprocks in the Barents Sea, the presented data are invaluable for structural, analogue, caprock appraisal, and fluid flow studies.

7 Appendix



Table A1: Flight counts, image ids, counts and other acquisition metadata. Flight metadata for flights 23-25 were disabled owing to inaccurate altitude recordings.

flight	image-ids	image-count	disabled	non-aligned	flight-date	weather
flight-01	im_0001-im_0280	280	-	im_0278, im_0280	24-07-2020	overcast
flight-02	im_0281-im_0559	279	-	im_0410, im_0411	24-07-2020	overcast
flight-03	im_0560-im_0770	211	im_0763, im_0764, im_0765, im_0770	im_0749, im_0766, im_0767, im_0768, im_0769	24-07-2020	overcast
flight-04	im_0771-im_1035	265	-	-	25-07-2020	overcast
flight-05	im_1036-im_1312	277	-	-	25-07-2020	overcast
flight-06	im_1313-im_1564	252	-	-	25-07-2020	overcast
flight-07	im_1565-im_1849	285	-	-	25-07-2020	overcast
flight-08	im_1850-im_2042	193	-	-	25-07-2020	overcast
flight-09	im_2043-im_2312	270	-	-	25-07-2020	overcast
flight-10	im_2313-im_2566	254	-	-	25-07-2020	overcast
flight-11	im_2567-im_2771	205	-	-	25-07-2020	overcast
flight-12	im_2772-im_2947	176	-	-	26-07-2020	overcast
flight-13	im_2948-im_3158	211	-	-	26-07-2020	overcast
flight-15	im_3159-im_3323	165	-	-	26-07-2020	overcast
flight-16	im_3324-im_3515	192	-	im_3502	08-08-2020	overcast
flight-17	im_3516-im_3729	214	-	-	08-08-2020	overcast
flight-18	im_3730-im_3964	235	-	-	08-08-2020	overcast
flight-19	im_3965-im_4202	238	-	-	09-08-2020	overcast
flight-20	im_4203-im_4385	183	-	im_4385	09-08-2020	overcast
flight-21	im_4386-im_4587	202	-	-	09-08-2020	overcast
flight-22	im_4588-im_4764	177	-	im_4750, im_4754	09-08-2020	overcast
flight-23	im_4765-im_5015	251	-	-	18-08-2020	mostly sunny
flight-24	im_5016-im_5267	252	-	-	18-08-2020	mostly sunny
flight-25	im_5268-im_5512	245	-	-	18-08-2020	mostly sunny



Table B1: Machine specifications of the machines used for the SfM photogrammetry processing.

No	Workstation type	Processor	Installed RAM	System Type	Windows Edition	Windows Version	OS-Build	Graphics card	Driver version	Metashape Version
AG-WS- Z6-01	HP Z6 G4	Intel®Xeon®Gold 5122 CPU @ 3.60GHz 3.59GHz	128 GB	64-bit	Windows 10 Enterprise	2004	19041,1110	NVIDIA Quadro P5000	27.21.14.5239	1.7.2.12040
AG-WS- Z6-02	HP Z1 Entry Tower G5	Intel®Core i9-9900K CPU @ 3.60GHz 3.60GHz	128 GB	64-bit	Windows 10 Enterprise	2004	19041,1110	NVIDIA GeForce RTX2080	27.21.14.6140	1.7.2.12040
AG-WS- Z6-03	HP Z1 Entry Tower G5	Intel®Core i9-9900K CPU @ 3.60GHz 3.60GHz	128 GB	64-bit	Windows 10 Enterprise	2004	19041,1110	NVIDIA GeForce RTX2080	27.21.14.5749	1.7.2.12040
AG-WS- Z1-01	HP Z1 Entry Tower G6	Intel®Core i9-10900K CPU @ 2.80GHz 2.81GHz	128 GB	64-bit	Windows 10 Enterprise	2004	19041,1110	NVIDIA GeForce RTX2080 SUPER		1.7.2.12040
AG-WS- Z1-02	HP Z1 Entry Tower G6	Intel®Core i9-10900K CPU @ 2.80GHz 2.81GHz	128 GB	64-bit	Windows 10 Enterprise	2004	19041,1110	NVIDIA GeForce RTX2080 SUPER		1.7.2.12040
AG-WS- Z1-03	HP Z1 Entry Tower G5	Intel®Core i9-9900K CPU @ 3.60GHz 3.60GHz	128 GB	64-bit	Windows 10 Enterprise	2004	19041,1052	NVIDIA GeForce RTX2080		1.7.2.12040



Table C1: Structural measurements and ground truthing as measured in 2021. Easting and Northing given in the WGS 84/UTM zone 33N (EPSG:32633) projection. The calculated orthogonal heights use the Earth Gravitational Model 2008 (Pavlis et al., 2008).

Point_ID	Point_Role	Strike	Dip	Northing (y, m)	Easting (x, m)	Altitude (m)	DTM (m)	Alt.-DTM (m)
KW-F0-STR_GPS0001	Code PP	-	-	8696460.286	518756.896	106.015	108.315	-2.299
KW-F0-STR_GPS0003	Code PP	-	-	8696458.301	518756.472	107.934	109.565	-1.632
KW-F0_GPS0001	Code PP	-	-	8696454.318	518754.515	111.002	112.414	-1.412
KW-F0_GPS0008	Code PP	-	-	8696328.256	518729.995	171.578	170.285	1.294
KW-F0_GPS0012	Code PP	-	-	8696457.052	518756.378	114.335	110.181	4.154
KW-F0_GPS0016-S341-D45	Code PP	STR341	DIP045	8696333.236	518729.75	167.34	167.944	-0.604
KW-F0_STR009-D64W	Code PP	STR009	DIP64W	8696310.002	518727.444	178.038	178.73	-0.693
KW-F0_STR017-D51W	Code PP	STR017	DIP51W	8696327.254	518730.066	169.742	170.652	-0.910
KW-F10_GPS0002	Code PP	-	-	8696423.945	518718.28	146.282	146.463	-0.180
KW-F10_GPS0003	Code PP	-	-	8696416.604	518720.209	146.21	147.017	-0.806
KW-F1_GPS0004	Code PP	-	-	8696472.47	518729.793	134.386	133.863	0.523
KW-F2_GPS0002	Code PP	-	-	8696433.364	518731.923	135.549	135.367	0.182
KW-F3_STR012-DIP55NW	Code PP	STR012	DIP55NW	8696270.747	518740.86	188.103	186.908	1.195
KW-F5_GPS0001	Code PP	-	-	8696293.142	518774.962	160.989	161.125	-0.136
KW-F5_GPS0003	Code PP	-	-	8696296.485	518768.454	164.148	164.321	-0.173
KW-F5_GPS0004	Code PP	-	-	8696292.058	518791.84	156.752	155.472	1.280
KW-F5_GPS0005	Code PP	-	-	8696334.989	518766.264	143.964	143.173	0.791
KW-F6_GPS0004	Code PP	-	-	8696242.727	518752.355	190.514	191.068	-0.553
KW-F7_GPS0004	Code PP	-	-	8696225.701	518771.544	190.349	190.142	0.207
Mean	Code PP	-	-	-	-	-	-	0.012
RMSE	Code PP	-	-	-	-	-	-	1.369
KW-F0-STR_GPS0002	Widelane PP	-	-	8696459.482	518757.275	108.021	108.052	-0.031
KW-F0_GPS00015	Widelane PP	STR354	DIP72NW	8696313.79	518728.98	176.296	176.881	-0.585
KW-F0_GPS0015	Widelane PP	-	-	8696342.655	518731.01	163.24	163.185	0.055
KW-F0_STR333-D22SW	Widelane PP	STR333	DIP022SW	8696306.097	518738.723	175.82	175.552	0.268
KW-F0_STR341-D24W	Widelane PP	STR341	DIP024W	8696315.672	518736.399	172.592	172.883	-0.292
KW-F0_STR356-D42W	Widelane PP	STR356	DIP042W	8696298.749	518740.577	177.18	177.275	-0.095
KW-F10_GPS0001	Widelane PP	-	-	8696433.977	518714.811	146.192	145.978	0.213
KW-F10_GPS0004	Widelane PP	-	-	8696401.999	518723.62	147.474	147.935	-0.461
KW-F10_GPS0007	Widelane PP	-	-	8696370.324	518727.928	154.16	153.553	0.607
KW-F10_GPS0008	Widelane PP	-	-	8696363.545	518728.592	155.543	155.464	0.078
KW-F10_STR053-50	Widelane PP	STR053	DIP050	8696383.281	518728.179	149.168	149.906	-0.738
KW-F4_GPS0006	Widelane PP	-	-	8696303.806	518756.864	170.092	170.147	-0.055
KW-F6_GPS0005	Widelane PP	-	-	8696241.224	518752.289	191.52	191.576	-0.056
KW-F7_GPS0002	Widelane PP	-	-	8696266.339	518796.147	166.891	166.776	0.115
KW-F7_GPS0005	Widelane PP	-	-	8696220.51	518766.392	191.298	191.651	-0.353
KW-F7_GPS0006	Widelane PP	-	-	8696217.741	518764.418	191.976	192.206	-0.230
KW-F8_GPS0001	Widelane PP	-	-	8696319.93	518745.222	166.139	166.704	-0.564
Mean	Widelane PP	-	-	-	-	-	-	-0.125
RMSE	Widelane PP	-	-	-	-	-	-	0.360
KW-F0-STR_GPS0004	Fixed PP	-	-	8696456.68	518755.911	110.41	110.573	-0.163
KW-F0_GPS0002	Fixed PP	-	-	8696448.839	518753.157	114.356	114.496	-0.140
KW-F0_GPS0003	Fixed PP	-	-	8696428.921	518749.878	121.365	121.825	-0.460
KW-F0_GPS0004	Fixed PP	-	-	8696416.751	518746.036	127.935	128.161	-0.226
KW-F0_GPS0005	Fixed PP	-	-	8696408.444	518746.003	131.095	131.539	-0.444
KW-F0_GPS0006	Fixed PP	-	-	8696353.24	518731.143	158.998	159.174	-0.177
KW-F0_GPS0007	Fixed PP	-	-	8696333.499	518729.948	167.343	167.729	-0.386
KW-F0_GPS0009	Fixed PP	-	-	8696319.408	518730.681	173.372	173.61	-0.238
KW-F0_GPS0010	Fixed PP	-	-	8696313.883	518729.056	176.824	176.79	0.034
KW-F0_GPS0011	Fixed PP	-	-	8696310.289	518727.653	178.823	178.573	0.250
KW-F0_GPS0013	Fixed PP	-	-	8696373.355	518732.689	149.41	149.713	-0.303
KW-F0_GPS0014	Fixed PP	-	-	8696369.258	518730.092	152.292	152.576	-0.284
KW-F0_STR024-D26W	Fixed PP	STR024	DIP026W	8696319.071	518730.498	173.817	173.842	-0.025
KW-F10_STR340-36W	Fixed PP	STR340	DIP036W	8696391.481	518726.555	148.327	148.693	-0.366
KW-F1_GPS0001	Fixed PP	-	-	8696450.341	518750.221	116.281	116.481	-0.200
KW-F1_GPS0002	Fixed PP	-	-	8696455.901	518742.946	120.727	120.817	-0.090
KW-F1_GPS0003	Fixed PP	-	-	8696461.142	518737.744	125.291	125.401	-0.110
KW-F1_GPS0005	Fixed PP	-	-	8696474.471	518728.393	134.914	135.054	-0.140
KW-F2_GPS0001	Fixed PP	-	-	8696431.43	518743.998	125.197	125.32	-0.123
KW-F2_GPS0003	Fixed PP	-	-	8696431.626	518736.309	131.819	132.035	-0.217
KW-F3_GPS0001	Fixed PP	-	-	8696315.864	518736.276	172.559	172.844	-0.286
KW-F3_GPS0002	Fixed PP	-	-	8696303.056	518739.512	176.009	176.232	-0.223



Point_ID	Point_Role	Strike	Dip	Northing (y, m)	Easting (x, m)	Altitude (m)	DTM (m)	Alt.-DTM (m)
KW-F3_GPS0003	Fixed PP	-	-	8696299.529	518740.468	176.935	177.009	-0.074
KW-F3_GPS0004	Fixed PP	-	-	8696283.223	518743.671	182.031	182.094	-0.063
KW-F3_GPS0005	Fixed PP	-	-	8696265.368	518739.263	188.907	189.154	-0.247
KW-F4_GPS0001	Fixed PP	-	-	8696326.876	518763.024	149.073	149.201	-0.127
KW-F4_GPS0002	Fixed PP	-	-	8696321.203	518761.815	153.853	153.968	-0.115
KW-F4_GPS0003	Fixed PP	-	-	8696311.897	518758.326	163.487	163.354	0.134
KW-F4_GPS0004	Fixed PP	-	-	8696306.988	518758.403	167.672	167.706	-0.034
KW-F4_GPS0005	Fixed PP	-	-	8696305.151	518757.505	169.132	169.226	-0.094
KW-F5_GPS0002	Fixed PP	-	-	8696296.34	518768.501	164.321	164.366	-0.044
KW-F6_GPS0001	Fixed PP	-	-	8696277.021	518785.938	165.738	165.861	-0.123
KW-F6_GPS0002	Fixed PP	-	-	8696276.514	518783.578	167.927	168.169	-0.242
KW-F6_GPS0003	Fixed PP	-	-	8696244.044	518752.62	190.219	190.548	-0.329
KW-F7_GPS0001	Fixed PP	-	-	8696269.317	518797.22	164.749	164.915	-0.166
KW-F7_GPS0003	Fixed PP	-	-	8696262.888	518794.998	168.751	168.882	-0.131
Mean	Fixed PP	-	-	-	-	-	-	-0.166
RMSE	Fixed PP	-	-	-	-	-	-	0.220



Author contributions

PB: Conceptualization, Data curation, Formal analysis, Funding acquisition, Investigation, Methodology, Project administration, Software, Validation, Visualization, Writing - original draft preparation; TB: Formal analysis, Investigation, Methodology, Validation, Writing - review & editing; GL: Formal analysis, Investigation, Validation, Writing - review & editing; SO: Formal analysis, Funding acquisition, Investigation, Methodology, Validation, Writing - review & editing; LN: Conceptualization, Funding acquisition, Investigation; KO: Conceptualization, Funding acquisition, Supervision, Visualization, Writing - review & editing; KS: Conceptualization, Funding acquisition, Supervision, Writing - review & editing.

Competing interests

The authors declare that they have no conflict of interest.

Acknowledgements

We sincerely appreciate the data provided by the UNIS CO₂ lab (<http://CO2-ccs.unis.no/>), and educational licenses provided by Schlumberger (Petrel), Cegal (Blueback plugins) and Advanced Logic Technology (WellCAD). We further thank our colleagues, in particular Nil Rodes, Aleksandra Smyrak-Sikora, Julian Janocha, Richard Hann, and Karoline Løvlie, for meaningful discussions and their support during three extensive field campaigns, some plagued by polar bears. This study was partly funded by the Norwegian CCS Research Centre (NCCS; industry partners and The Research Council of Norway (RCN) #257579), and the Research Centre for Arctic Petroleum Exploration (ARCEX; industry partners and RCN #228107), in addition to three Svalbard Science Forum Arctic Field Grants (RCN #295627, #310638, and #322259).



References

- 375 Barnes, R., Gupta, S., Traxler, C., Ortner, T., Bauer, A., Hesina, G., Paar, G., Huber, B., Juhart, K., Fritz, L., Nauschnegg, B., Muller, J.-P., and Tao, Y.: Geological Analysis of Martian Rover-Derived Digital Outcrop Models Using the 3-D Visualization Tool, Planetary Robotics 3-D Viewer—PRo3D, *Earth and Space Science*, 5, 285–307, <https://doi.org/10.1002/2018EA000374>, 2018.
- Bergh, S. G., Braathen, A., and Andresen, A.: Interaction of Basement-Involved and Thin-Skinned Tectonism in the Tertiary Fold-Thrust Belt of Central Spitsbergen, Svalbard1, *AAPG Bulletin*, 81, 637–661, <https://doi.org/10.1306/522B43F7-1727-11D7-8645000102C1865D>,
380 1997.
- Betlem, P.: PeterBetlem/Automated_metashape: Package Release v0.1.12 - Automated Metashape, Zenodo [code], <https://doi.org/10.5281/zenodo.6448154>, 2022a.
- Betlem, P.: Svalbox-DOM_2020-0039, Norstore [data set], <https://doi.org/10.11582/2022.00027>, 2022b.
- Betlem, P.: Svalbox-DOM_2020-0039: Supplementary Material and Processing Examples, Zenodo [code],
385 <https://doi.org/10.5281/zenodo.6497417>, 2022c.
- Bilmes, A., D’Elia, L., Lopez, L., Richiano, S., Varela, A., Alvarez, M. d. P., Bucher, J., Eymard, I., Muravchik, M., Franzese, J., and Ariztegui, D.: Digital Outcrop Modelling Using “Structure-from-Motion” Photogrammetry: Acquisition Strategies, Validation and Interpretations to Different Sedimentary Environments, *Journal of South American Earth Sciences*, 96, 102 325, <https://doi.org/10.1016/j.jsames.2019.102325>, 2019.
- 390 Birchall, T., Senger, K., Hornum, M., Olaussen, S., and Braathen, A.: Underpressure of the Barents Shelf: Causes and Implications for Hydrocarbon Exploration, *AAPG Bulletin*, <https://doi.org/10.1306/02272019146>, 2020.
- Braathen, A., Bergh, S. G., and Maher Jr., H. D.: Structural Outline of a Tertiary Basement-cored Uplift/Inversion Structure in Western Spitsbergen, Svalbard: Kinematics and Controlling Factors, *Tectonics*, 14, 95–119, <https://doi.org/10.1029/94TC01677>, 1995.
- Braathen, A., Berc, S. G., and Maher, H. D.: Thrust Kinematics in the Central Part of the Tertiary Transpressional Fold-Thrust Belt in
395 Spitsbergen, *Geological Survey of Norway*, 433, 32–33, 1997.
- Braathen, A., Bælum, K., Christiansen, H. H., Dahl, T., Eiken, O., Elvebakk, H., Hansen, F., Hanssen, T. H., Jochmann, M., and Johansen, T. A.: The Longyearbyen CO2 Lab of Svalbard, Norway—Initial Assessment of the Geological Conditions for CO2 Sequestration, *Norwegian Journal of Geology*, 92, 353–376, 2012.
- Bradski, G.: The OpenCV Library, *Dr. Dobb’s Journal of Software Tools*, 2000.
- 400 Buckley, S. J., Ringdal, K., Naumann, N., Dolva, B., Kurz, T. H., Howell, J. A., and Dewez, T. J.: LIME: Software for 3-D Visualization, Interpretation, and Communication of Virtual Geoscience Models, *Geosphere*, 15, 222–235, <https://doi.org/10.1130/GES02002.1>, 2019.
- Buckley, S. J., Howell, J. A., Naumann, N., Lewis, C., Chmielewska, M., Ringdal, K., Vanbiervliet, J., Tong, B., Mulelid-Tynes, O. S., Foster, D., Maxwell, G., and Pugsley, J.: V3Geo: A Cloud-Based Repository for Virtual 3D Models in Geoscience, *Geoscience Communication*, 5, 67–82, <https://doi.org/10.5194/gc-5-67-2022>, 2022.
- 405 Burnham, B. S., Bond, C., Flaig, P. P., van der Kolk, D. A., and Hodgetts, D.: Outcrop Conservation: Promoting Accessibility, Inclusivity, and Reproducibility through Digital Preservation, *The Sedimentary Record*, 20, 5–14, 2022.
- Butler, H., Chambers, B., Hartzell, P., and Glennie, C.: PDAL: An Open Source Library for the Processing and Analysis of Point Clouds, *Computers & Geosciences*, 148, 104 680, <https://doi.org/10.1016/j.cageo.2020.104680>, 2021.
- Cawood, A. J. and Bond, C. E.: eRock: An Open-Access Repository of Virtual Outcrops for Geoscience Education, *GSA today*, 28, 36–37,
410 2019.



- Collignon, M. and Hammer, Ø.: Petrography and Sedimentology of the Slottsmøya Member at Janusfjellet, Central Spitsbergen., Norwegian Journal of Geology/Norsk Geologisk Forening, 92, 89–101, 2012.
- Cramer, F., Shephard, G. E., and Heron, P. J.: The Misuse of Colour in Science Communication, *Nature Communications*, 11, 5444, <https://doi.org/10.1038/s41467-020-19160-7>, 2020.
- 415 Dering, G. M., Micklethwaite, S., Thiele, S. T., Vollgger, S. A., and Cruden, A. R.: Review of Drones, Photogrammetry and Emerging Sensor Technology for the Study of Dykes: Best Practises and Future Potential, *Journal of Volcanology and Geothermal Research*, 373, 148–166, <https://doi.org/10.1016/j.jvolgeores.2019.01.018>, 2019.
- Dypvik, H. and Harris, N. B.: Geochemical Facies Analysis of Fine-Grained Siliciclastics Using Th/U, Zr/Rb and (Zr+Rb)/Sr Ratios, *Chemical Geology*, 181, 131–146, [https://doi.org/10.1016/S0009-2541\(01\)00278-9](https://doi.org/10.1016/S0009-2541(01)00278-9), 2001.
- 420 Dypvik, H., Eikeland, T. A., Backer-Owe, K., Andresen, A., Johansen, H., Elverhøy, A., Nagy, J., Haremo, P., and Bierke, T.: The Janusfjellet Subgroup (Bathonian to Hauterivian) on Central Spitsbergen: A Revised Lithostratigraphy, *Polar Research*, 9, 21–44, <https://doi.org/10.1111/j.1751-8369.1991.tb00400.x>, 1991.
- Garrido-Jurado, S., Muñoz-Salinas, R., Madrid-Cuevas, F. J., and Marín-Jiménez, M. J.: Automatic Generation and Detection of Highly Reliable Fiducial Markers under Occlusion, *Pattern Recognition*, 47, 2280–2292, <https://doi.org/10.1016/j.patcog.2014.01.005>, 2014.
- 425 Grundvåg, S. A., Marin, D., Kairanov, B., Śliwińska, K. K., Nøhr-Hansen, H., Jelby, M. E., Escalona, A., and Olaussen, S.: The Lower Cretaceous Succession of the Northwestern Barents Shelf: Onshore and Offshore Correlations, *Marine and Petroleum Geology*, 86, 834–857, <https://doi.org/10.1016/j.marpetgeo.2017.06.036>, 2017.
- Harland, W. B., Anderson, L. M., Manasrah, D., Butterfield, N. J., Challinor, A., Doubleday, P. A., Dowdeswell, E. K., Dowdeswell, J. A., Geddes, I., Kelly, S. R., et al.: *The Geology of Svalbard*, vol. 17, Geological Society London, 1997.
- 430 Harrald, J. E. G., Coe, A. L., Thomas, R. M., and Hoggett, M.: Use of Drones to Analyse Sedimentary Successions Exposed in the Foreshore, *Proceedings of the Geologists' Association*, 132, 253–268, <https://doi.org/10.1016/j.pgeola.2021.02.001>, 2021.
- Healy, D., Rizzo, R. E., Cornwell, D. G., Farrell, N. J. C., Watkins, H., Timms, N. E., Gomez-Rivas, E., and Smith, M.: FracPaQ: A MATLAB™ Toolbox for the Quantification of Fracture Patterns, *Journal of Structural Geology*, 95, 1–16, <https://doi.org/10.1016/j.jsg.2016.12.003>, 2017.
- 435 Henriksen, E., Ryseth, A. E., Larssen, G. B., Heide, T., Rønning, K., Sollid, K., and Stoupakova, A. V.: Chapter 10 Tectonostratigraphy of the Greater Barents Sea: Implications for Petroleum Systems, Geological Society, London, *Memoirs*, 35, 163–195, <https://doi.org/10.1144/M35.10>, 2011.
- Hiep, V. H., Keriven, R., Labatut, P., and Pons, J.-P.: Towards High-Resolution Large-Scale Multi-View Stereo, in: *IEEE Conference on Computer Vision and Pattern Recognition (20-25 June 2009)*, pp. 1430–1437, IEEE, Miami, FL, USA, 2009.
- 440 Hirschmuller, H.: Stereo Processing by Semiglobal Matching and Mutual Information, *IEEE Transactions on pattern analysis and machine intelligence*, 30, 328–341, 2007.
- Howell, J. A., Martinius, A. W., and Good, T. R.: The Application of Outcrop Analogues in Geological Modelling: A Review, Present Status and Future Outlook, Geological Society, London, *Special Publications*, 387, 1–25, <https://doi.org/10.1144/SP387.12>, 2014.
- Humlum, O., Instanes, A., and Sollid, J. L.: Permafrost in Svalbard: A Review of Research History, Climatic Background and Engineering Challenges, *Polar Research*, 22, 191–215, <https://doi.org/10.1111/j.1751-8369.2003.tb00107.x>, 2003.
- 445 Huq, F., Smalley, P. C., Mørkvad, P. T., Johansen, I., Yarushina, V., and Johansen, H.: The Longyearbyen CO₂ Lab: Fluid Communication in Reservoir and Caprock, *International Journal of Greenhouse Gas Control*, 63, 59–76, <https://doi.org/10.1016/j.ijggc.2017.05.005>, 2017.



- James, M. R., Chandler, J. H., Eltner, A., Fraser, C., Miller, P. E., Mills, J. P., Noble, T., Robson, S., and Lane, S. N.: Guidelines on the Use of Structure-from-Motion Photogrammetry in Geomorphic Research, *Earth Surface Processes and Landforms*, 44, 2081–2084, 450 <https://doi.org/10.1002/esp.4637>, 2019.
- Kingsland, K.: Comparative Analysis of Digital Photogrammetry Software for Cultural Heritage, *Digital Applications in Archaeology and Cultural Heritage*, 18, e00157, <https://doi.org/10.1016/j.daach.2020.e00157>, 2020.
- Koevoets, M. J., Abay, T. B., Hammer, Ø., and Olaussen, S.: High-Resolution Organic Carbon–Isotope Stratigraphy of the Middle Jurassic–Lower Cretaceous Agardhfjellet Formation of Central Spitsbergen, Svalbard, *Palaeogeography, Palaeoclimatology, 455 Palaeoecology*, 449, 266–274, <https://doi.org/10.1016/j.palaeo.2016.02.029>, 2016.
- Koevoets, M. J., Hammer, Ø., Olaussen, S., Senger, K., and Smelror, M.: Integrating Subsurface and Outcrop Data of the Middle Jurassic to Lower Cretaceous Agardhfjellet Formation in Central Spitsbergen, *Norsk Geologisk Tidsskrift*, 98, <https://doi.org/10.17850/njg98-4-01>, 2018.
- Koevoets, M. K., Hammer, Ø., and Little, C. T. S.: Palaeoecology and Palaeoenvironments of the Middle Jurassic to Lowermost Cretaceous 460 Agardhfjellet Formation (Bathonian–Ryazanian), Spitsbergen, Svalbard, *Norwegian Journal of Geology*, 99, 2019.
- Leica Geosystems AG: Leica Viva GS16 Data Sheet.
- Leon, J. X., Heuvelink, G. B. M., and Phinn, S. R.: Incorporating DEM Uncertainty in Coastal Inundation Mapping, *PLOS ONE*, 9, e108727, <https://doi.org/10.1371/journal.pone.0108727>, 2014.
- Løvlie, K. H.: Structural Deformation and Mineralogy of the Agardhfjellet and Rurikfjellet Formations in Central Spitsbergen, Svalbard, 465 MSc, University of Oslo, Oslo, 2020.
- Marques, A., Horota, R. K., de Souza, E. M., Kupssinskü, L., Rossa, P., Aires, A. S., Bachi, L., Veronez, M. R., Gonzaga, L., and Cazarin, C. L.: Virtual and Digital Outcrops in the Petroleum Industry: A Systematic Review, *Earth-Science Reviews*, 208, 103260, <https://doi.org/10.1016/j.earscirev.2020.103260>, 2020.
- Mørk, A., Dallmann, W. K., Dypvik, H., Johannessen, E. P., Larssen, G. B., Nagy, J., Nøttvedt, A., Olaussen, S., Pchelina, T. M., and 470 Worsley, D.: Mesozoic Lithostratigraphy, Lithostratigraphic lexicon of Svalbard. Upper Palaeozoic to Quaternary bedrock. Review and recommendations for nomenclature use, pp. 127–214, 1999.
- Mulrooney, M. J., Larsen, L., Van Stappen, J. F., Rismyhr, B., Senger, K., Braathen, A., Olaussen, S., Mørk, M. B. E., Ogata, K., and Cnudde, V.: Fluid Flow Properties of the Wilhelmøya Subgroup, a Potential Unconventional CO₂ Storage Unit in Central Spitsbergen, *Norwegian Journal of Geology*, 99, 85–116, <https://doi.org/10.17850/njg002>, 2018.
- 475 Nakken, L.: Structural Evolution of the Lower Agardhfjellet Formation, in Central Spitsbergen: Implications for Caprock Integrity, MSc, University of Oslo, Oslo, Norway, 2020.
- Norwegian Polar Institute: Terrengmodell Svalbard (S0 Terrengmodell), <https://doi.org/10.21334/NPOLAR.2014.DCE53A47>, 2014.
- Norwegian Polar Institute: Geological Map of Svalbard (1:250000), <https://doi.org/10.21334/NPOLAR.2016.616F7504>, 2016.
- Norwegian Polar Institute: NP_Ortofoto_Svalbard_WMTS_25833 [Dataset], 2017.
- 480 Ogata, K., Senger, K., Braathen, A., Tveranger, J., and Olaussen, S.: The Importance of Natural Fractures in a Tight Reservoir for Potential CO₂ Storage: A Case Study of the Upper Triassic–Middle Jurassic Kapp Toscana Group (Spitsbergen, Arctic Norway), *Geological Society, London, Special Publications*, 374, 395–415, <https://doi.org/10.1144/SP374.9>, 2012.
- Ogata, K., Senger, K., Braathen, A., Tveranger, J., and Olaussen, S.: Fracture Systems and Mesoscale Structural Patterns in the Siliciclastic Mesozoic Reservoir–Caprock Succession of the Longyearbyen CO₂ Lab Project: Implications for Geological CO₂ Sequestration in Central 485 Spitsbergen, Svalbard, *Norwegian Journal of Geology*, pp. 121–154, 2014.



- Olaussen, S., Senger, K., Braathen, A., Grundvåg, S.-A., and Mørk, A.: You Learn as Long as You Drill; Research Synthesis from the Longyearbyen CO2 Laboratory, Svalbard, Norway., 157–187, <https://doi.org/10.17850/njg008>, 2019.
- Over, J.-S. R., Ritchie, A. C., Kranenburg, C. J., Brown, J. A., Buscombe, D. D., Noble, T., Sherwood, C. R., Warrick, J. A., and Wernette, P. A.: Processing Coastal Imagery with Agisoft Metashape Professional Edition, Version 1.6—Structure from Motion Workflow Documentation, Tech. rep., US Geological Survey, 2021.
- Pavlis, N., Kenyon, S., Factor, J., and Holmes, S.: Earth Gravitational Model 2008, in: SEG Technical Program Expanded Abstracts 2008, SEG Technical Program Expanded Abstracts, pp. 761–763, Society of Exploration Geophysicists, <https://doi.org/10.1190/1.3063757>, 2008.
- PDAL Contributors: PDAL Point Data Abstraction Library, Zenodo [code], <https://doi.org/10.5281/zenodo.2556738>, 2018.
- 495 Rippin, D. M., Pomfret, A., and King, N.: High Resolution Mapping of Supra-Glacial Drainage Pathways Reveals Link between Micro-Channel Drainage Density, Surface Roughness and Surface Reflectance, *Earth Surface Processes and Landforms*, 40, 1279–1290, <https://doi.org/10.1002/esp.3719>, 2015.
- Rizzo, R. E., Fazeli, H., Maier, C., March, R., Egya, D., Doster, F., Kubeyev, A., Kampman, N., Bisdorn, K., Snippe, J., Senger, K., Betlem, P., Phillips, T., Inskip, N. F., Esegue, O., and Busch, A.: Understanding Fault and Fracture Networks to De-Risk Geological Leakage from Subsurface Storage Sites, in: 1st Geoscience & Engineering in Energy Transition Conference, vol. 2020, pp. 1–5, European Association of Geoscientists & Engineers, <https://doi.org/10.3997/2214-4609.202021016>, 2020.
- 500 Rizzo, R. E., Fazeli, H., Doster, F., Kampman, N., Bisdorn, K., Snippe, J., Senger, K., Betlem, P., and Busch, A.: Role of Fault and Fracture Networks to De-Risk Geological Leakage from Subsurface Energy Sites, pp. EGU21–8517, 2021.
- Rouault, E., Warmerdam, F., Schwehr, K., Kiselev, A., Butler, H., Łoskot, M., Szekeres, T., Tourigny, E., Landa, M., Miara, I., Elliston, B., Kumar, C., Plesea, L., Morissette, D., Jolma, A., and Dawson, N.: GDAL, Zenodo [code], <https://doi.org/10.5281/zenodo.6352176>, 2022.
- 505 Schaaf, N. W., Senger, K., Mulrooney, M. J., Ogata, K., Braathen, A., and Olaussen, S.: Towards Characterization of Natural Fractures in a Caprock Shale: An Integrated Borehole-Outcrop Study of the Agardhfjellet Formation, Svalbard, Arctic Norway, in: Norwegian Geological Society Winter Conference, Oslo, <https://doi.org/10.13140/RG.2.2.23744.74249/1>, 2017.
- Senger, K., Tveranger, J., Ogata, K., Braathen, A., and Planke, S.: Late Mesozoic Magmatism in Svalbard: A Review, *Earth-Science Reviews*, 510 139, 123–144, <https://doi.org/10.1016/j.earscirev.2014.09.002>, 2014.
- Senger, K., Buckley, S. J., Chevallier, L., Fagereng, Å., Galland, O., Kurz, T. H., Ogata, K., Planke, S., and Tveranger, J.: Fracturing of Doleritic Intrusions and Associated Contact Zones: Implications for Fluid Flow in Volcanic Basins, *Journal of African Earth Sciences*, 102, 70–85, <https://doi.org/10.1016/j.jafrearsci.2014.10.019>, 2015.
- 515 Senger, K., Brugmans, P., Grundvåg, S.-A., Jochmann, M., Nøttvedt, A., Olaussen, S., Skotte, A., and Smyrak-Sikora, A.: Petroleum, Coal and Research Drilling Onshore Svalbard: A Historical Perspective, *Norwegian Journal of Geology*, 99, <https://doi.org/10.17850/njg99-3-1>, 2019.
- Senger, K., Betlem, P., Birchall, T., Buckley, S. J., Coakley, B., Eide, C. H., Flaig, P. P., Forien, M., Galland, O., Gonzaga, L., Jensen, M., Kurz, T., Lecomte, I., Mair, K., Malm, R. H., Mulrooney, M., Naumann, N., Nordmo, I., Nolde, N., Ogata, K., Rabbel, O., Schaaf, N. W., and Smyrak-Sikora, A.: Using Digital Outcrops to Make the High Arctic More Accessible through the Svalbox Database, *Journal of Geoscience Education*, 69, 123–137, <https://doi.org/10.1080/10899995.2020.1813865>, 2021.
- 520 Sibson, R. H.: Structural Permeability of Fluid-Driven Fault-Fracture Meshes, *Journal of Structural Geology*, 18, 1031–1042, [https://doi.org/10.1016/0191-8141\(96\)00032-6](https://doi.org/10.1016/0191-8141(96)00032-6), 1996.



- Smith, M., Carrivick, J., and Quincey, D.: Structure from Motion Photogrammetry in Physical Geography, *Progress in Physical Geography: Earth and Environment*, 40, 247–275, <https://doi.org/10.1177/0309133315615805>, 2016.
- 525 Spencer, A. M., Briskeby, P. I., Christensen, L. D., Foyn, R., Kjolleberg, M., Kvasdheim, E., Knight, I., Rye-Larsen, M., and Williams, J.: Petroleum Geoscience in Norden-exploration, Production and Organization, *Episodes*, 31, 115–124, 2008.
- Stevens, J.-L. R., Rudiger, P., and Bednar, J. A.: HoloViews: Building Complex Visualizations Easily for Reproducible Science, in: *Proceedings of the 14th Python in Science Conference*, pp. 61–69, Citeseer, 2015.
- Tinkham, W. T. and Swayze, N. C.: Influence of Agisoft Metashape Parameters on UAS Structure from Motion Individual Tree Detection
530 from Canopy Height Models, *Forests*, 12, 250, <https://doi.org/10.3390/f12020250>, 2021.
- Tonkin, T. N., Midgley, N. G., Cook, S. J., and Graham, D. J.: Ice-Cored Moraine Degradation Mapped and Quantified Using an Unmanned Aerial Vehicle: A Case Study from a Polythermal Glacier in Svalbard, *Geomorphology*, 258, 1–10, <https://doi.org/10.1016/j.geomorph.2015.12.019>, 2016.
- Vieira, G., Mora, C., Pina, P., Ramalho, R., and Fernandes, R.: UAV-based Very High Resolution Point Cloud, Digital Surface
535 Model and Orthomosaic of the Chã Das Caldeiras Lava Fields (Fogo, Cabo Verde), *Earth System Science Data*, 13, 3179–3201, <https://doi.org/10.5194/essd-13-3179-2021>, 2021.
- Vollgger, S. A. and Cruden, A. R.: Mapping Folds and Fractures in Basement and Cover Rocks Using UAV Photogrammetry, Cape Liptrap and Cape Paterson, Victoria, Australia, *Journal of Structural Geology*, 85, 168–187, <https://doi.org/10.1016/j.jsg.2016.02.012>, 2016.
- Westoby, M. J., Brasington, J., Glasser, N. F., Hambrey, M. J., and Reynolds, J. M.: ‘Structure-from-Motion’ Photogrammetry: A Low-Cost,
540 Effective Tool for Geoscience Applications, *Geomorphology*, 179, 300–314, <https://doi.org/10.1016/j.geomorph.2012.08.021>, 2012.
- Zhou, Y., Daakir, M., Rupnik, E., and Pierrot-Deseilligny, M.: A Two-Step Approach for the Correction of Rolling Shutter Distortion in UAV Photogrammetry, *ISPRS Journal of Photogrammetry and Remote Sensing*, 160, 51–66, <https://doi.org/10.1016/j.isprsjprs.2019.11.020>, 2020.